

UNCLASSIFIED



Australian Government

Department of Defence

Defence Science and
Technology Organisation

XPAR-2 Search Mode Initial Design

T.V. Cao

National Security and ISR Division

Defence Science and Technology Organisation

DSTO-TR-2904

ABSTRACT

In this report, the initial design of a search mode for the Experimental Phased-Array Radar 2 (XPAR-2) system developed at DSTO is addressed. A track-while-scan search method combined with a one-step detection algorithm is proposed for implementation. Effects of discrete and distributed land clutter on detection performance are analysed. Limitation of clutter attenuation due to oscillator phase noise is addressed.

Three options for waveform and pulse repetition frequency (PRF) selections are considered. Option 1 consists of 8 PRFs which are designed for detection of targets between 2 NM to 20 NM. Option 2 consists of two separate PRF sets (each consists of 8 PRFs), which are designed such that one is optimised for close range targets between 2 NM to 7 NM, and one is optimised for targets between 7 NM to 20 NM. Option 3 is similar to option 1, but with twice the coherence processing interval. In all three options, the 3-of-8 binary detection rule is applied. Option 3 is selected for initial implementation.

A track-while-scan search regime combined with a sequential alert-confirm detection algorithm is considered for future research study.

APPROVED FOR PUBLIC RELEASE

UNCLASSIFIED

Published by

DSTO Defence Science and Technology Organisation

PO Box 1500

Edinburgh, South Australia 5111, Australia

Telephone: (08) 7389 5555

Facsimile: (08) 7389 6567

© Commonwealth of Australia 2013

AR No. AR-015-766

November, 2013

APPROVED FOR PUBLIC RELEASE

XPAR-2 Search Mode Initial Design

Executive Summary

A radar system performs multiple functions to cover many required applications. Two of the basic functions are search and track. The initial design of the search mode for the Experimental Phased-Array Radar 2 (XPAR-2) system developed at DSTO is addressed in this report.

The XPAR-2 is a ground-based radar system located at the Sensor Trials Facility (STF) adjacent to the Edinburgh airfield. The system consists of an L-band 8×8 array active aperture antenna, multiple IF receivers, analogue signal digitisers with high speed connection to general purpose computers, a multi-mode controller, and a graphical user interface (GUI) operator console.

A track-while-scan search regime, a one-step detection algorithm, and a simple beam scheduling algorithm in which the scan pattern is initially established and is never modified are selected for initial implementation.

The search mode is designed to cover a volume specified by an azimuth sector of 90 degrees, out to a maximum range of 20 NM, and an elevation sector which is shaped to give a detection contour at a constant altitude. The search for new targets is performed in two dimensions (2-D), i.e., azimuth search only. The targets of interest are small aircraft with radar cross-section (RCS) between 1 m^2 to 10 m^2 at ranges up to 7 NM, and large commercial aircraft with RCS of approximately 100 m^2 at ranges between 15 NM to 20 NM. The maximum target velocity is Mach-1 (approximately 340 m/s), while the maximum target acceleration is $2g$.

The structure of the search operation for XPAR-2 application is proposed. An analysis of the search performance from a radar detection perspective is presented. Since the efficiency of a detection algorithm depends on the clutter input level and clutter attenuation, limitation of clutter attenuation due to oscillator phase noise is addressed. Clutter input level due to distributed land clutter, distributed hill clutter, and discrete land clutter are also characterised.

In order to resolve range and velocity ambiguities, the 3-of-8 combination rule is employed. Three options for waveform and pulse repetition frequency (PRF) selections are presented. Option 1 consists of 8 PRFs which are designed for detection of targets between 2 NM to 20 NM. Option 2 consists of two separate PRF sets (each set consists of 8 PRFs), which are designed such that one is optimised for close range targets between 2 NM to 7 NM, and one is optimised for targets between 7 NM to 20 NM. Option 3 is similar to option 1, but with twice the coherent processing interval. Option 3 is proposed for initial implementation.

A track-while-scan search regime combined with a sequential alert-confirm detection algorithm is proposed for future research study. A beam scheduling algorithm, which maximises target detection probability while maintaining the frame-time to a minimum and subjects to bounded tracking errors, is worthwhile for investigation.

THIS PAGE IS INTENTIONALLY BLANK

Author

**Tri-Tan Van Cao***Electronic Warfare and Radar Division*

Tri-Tan Van Cao graduated from Flinders University, South Australia with a Bachelor of Biomedical Engineering (1998), and a Ph.D. in Electrical Engineering (2002) specialising in Nonlinear Automatic Control. He has been with DSTO since 2002, working mainly in the area of radar *constant false alarm rate* (CFAR) detection.

THIS PAGE IS INTENTIONALLY BLANK

Contents

1	Introduction.	1
1.1	Search Regimes.	1
1.2	Detection Regimes.	2
1.3	Beam Scheduling Regimes.	3
1.4	Scope of this Work.	4
2	Description of the XPAR-2 System.	4
3	Search Volume.	5
3.1	Elevation Coverage of an Antenna Beam.	5
3.2	Azimuth Coverage of an Antenna Beam.	5
4	Search Mode Operation.	7
4.1	Search Operation.	7
4.2	Track-while-Scan Processing.	9
4.3	Guard Channel Operation.	10
4.4	Measurements.	10
4.4.1	Measurement of Range and Velocity.	10
4.4.2	Measurement of Azimuth Angle.	11
4.4.3	Measurement Uncertainty.	12
5	Signal Processing.	13
6	CFAR Detection and Binary Detection.	15
6.1	Computation of Target Signal-to-Noise Ratio.	16
6.2	CA-CFAR Detection.	16
6.2.1	Description of the CA-CFAR Detector.	18
6.2.2	CA-CFAR False Alarm Rate and Detection Probability.	18
6.3	M -of- N Binary Detection.	19
7	Waveform & PRF Design.	20
7.1	Waveform Design.	21
7.2	PRF Selection.	22
7.3	Carrier Frequency Selection.	23

8	Results.	24
8.1	Case 1.	25
8.1.1	Search Operation.	25
8.1.2	PRF and Waveform Selection.	25
8.2	Case 2.	25
8.2.1	Search Operation.	25
8.2.2	PRF and Waveform Selection.	28
8.3	Case 3.	28
8.3.1	Search Operation.	28
8.3.2	PRF and Waveform Selection.	33
8.4	Target Detection Probability.	33
9	Dynamic Range.	39
9.1	Effect of Oscillator Phase Noise.	39
9.2	Effect of Clutter.	40
9.2.1	Overview of Constant- γ Clutter Model.	40
9.2.2	Discrete Ground Clutter.	41
9.2.3	Distributed Ground Clutter.	43
9.2.4	Distributed Hill Clutter.	46
9.3	Comparison of Three PRF Cases.	49
9.4	Summary.	50
10	Effect of a Sparse Array.	50
11	Alert-Confirm Search.	53
11.1	Search Operation.	54
11.2	Beam Scheduling.	54
11.3	Track-while-Scan Processing.	56
11.3.1	Alert Processing.	56
11.3.2	Confirm Processing.	57
11.4	False Alarm Rate & CA-CFAR Detection Threshold.	57
11.5	Computation of Target Detection Probability.	59
11.6	Waveforms and PRFs Design.	60
11.7	Comparison of One-step and Two-step Detectors.	60
11.7.1	Detection Performance.	61
11.7.2	Beam Scheduling Complexity.	61

12	Conclusions.	61
-----------	---------------------	-----------

Appendices

A	Computation of the Longest CPI.	64
B	Experimental Phase Noise.	65
C	Parameters of Land Surface.	66
D	Computation of Hill Clutter Area and Grazing Angle.	67
E	Alert-Confirm Waveform and PRF Parameters.	70
F	An Illustration Example of Alert-Confirm Beam Scheduling.	74
	References	77

Figures

1	Geographic coverage of XPAR-2 radar	6
2	XPAR-2 search volume.	7
3	Nine azimuth beams per scan for search mode operation.	8
4	Overview of search mode operation.	9
5	Overview of track-while-scan signal processing.	11
6	Concept of a guard channel.	12
7	Signal processing and detection at each beam position.	14
8	Signal Processing of one CPI.	15
9	Description of the CA-CFAR Detector.	18
10	Detection probability for selection of CFAR window length.	19
11	M-of-N selection.	21
12	Pulse repetition frequencies versus maximum unambiguous range and maximum unambiguous velocity.	24
13	Range blind-zone plot of case 1.	26
14	Velocity blind-zone plot of case 1.	27
15	Range-velocity blind-zone plot of case 1.	27
16	Range blind-zone plot of case 2, PRF set 1.	29
17	Velocity blind-zone plot of case 2, PRF set 1.	30
18	Range-velocity blind-zone plot of case 2, PRF set 1.	30
19	Range blind-zone plot of case 2, PRF set 2.	31
20	Velocity blind-zone plot of case 2, PRF set 2.	32
21	Range-velocity blind-zone plot of case 2, PRF set 2.	32
22	Range blind-zone plot of case 3.	34
23	Velocity blind-zone plot of case 3.	34
24	Range-velocity blind-zone plot of case 3.	35
25	Target detection probability of three cases with 8 clear PRFs.	37
26	Target SNR for RCS of 1, 10, and 100 m ²	37
27	Cases 1 & 2 target detection probability with different number of clear PRFs.	38
28	Case-3 target detection probability with different number of clear PRFs.	38
29	Limitation of clutter attenuation due to phase noise.	40
30	Land clutter reflectivity σ_{total}^0 at frequency 1.3 GHz.	42
31	Discrete clutter CNR and the corresponding received power, $CPI = 0.019$ s.	44

32	Ground-based radar clutter geometry.	44
33	Ground-based radar hill clutter geometry.	46
34	Top-view of hill clutter geometry.	47
35	Hill clutter geometry in 3D view.	48
36	Distributed CNR and received power.	49
37	Array configurations.	51
38	Sum channel beamforming with five antenna array columns (weights: 0.4827, 1.0000, 1.0000, 0.4827, 0.01).	52
39	Target detection probability for array configuration (i), with 8 clear PRFs. . .	53
40	Overview of search mode operation with a two-step sequential detector. . . .	56
41	Overview of track-while-scan search with an alert-confirm detector.	57
42	Alert-confirm target probability of detection.	60
43	One-step detection vs two-step detection at one false alarm per minute. . . .	62
44	One-step detection vs two-step detection with the same velocity resolution. .	62
B1	An experimental oscillator phase noise spectrum [21].	65
D1	Hill clutter geometry in 3-D view.	67
D2	Hill clutter geometry with grazing angle.	69
E1	Range blind-zone plot of major PRFs.	71
E2	Velocity blind-zone plot of major PRFs.	72
E3	Range blind-zone plot of major-minor PRFs.	73

THIS PAGE IS INTENTIONALLY BLANK

1 Introduction.

The initial design of a search mode for the Experimental Phased-Array Radar 2 (XPAR-2) system developed at DSTO is addressed in this report. In this introductory section, a general design analysis is presented, and the scope of the work is defined.

A radar system performs multiple functions to cover many required applications. Two of the basic functions are search and track. The radar search mode refers to the process of target detection without a priori knowledge of target existence, while target tracking refers to the process of collecting radar measurements and partitioning the measurements into sets of observations produced by the same sources [1], [2].

The radar search mode is designed to search for a given type of target in a specified search volume within a specified amount of time. The search volume is defined as a solid angle limited by an azimuth sector, an elevation sector, and out to a required maximum range. The frame-time, which is defined as the time it takes the antenna beam to completely scan through the search volume, should be short enough such that no targets of interest can completely go through, or be within the search volume for a long time without being detected. The frame-time can also be driven by track update requirement.

The targets of interest are specified by their radar cross-sections (RCS), their maximum velocity (Mach-1 for XPAR-2 application), and their maximum acceleration ($2g$ for XPAR-2 application). The output of the search mode is the number of new targets and target measurements which include target range, azimuth angle, elevation angle, velocity, and measurement uncertainties.

The design of a search mode involves (i) the selection of a search regime, (ii) the selection a detection regime, and (iii) the selection of a beam scheduling algorithm.

1.1 Search Regimes.

In a radar system equipped with an electronically scanned antenna (ESA) such as the XPAR-2, the radar can perform multiple functions almost simultaneously. In this case, the search and track functions can be combined to improve performance efficiency. There are three main approaches to the interleaving of the search and track functions: the track-while-scan (TWS), the search-and-track (SAT), and a combination of TWS and SAT [1].

In the TWS approach, the antenna scans with a pre-defined pattern which is never modified during search operation. If a target is detected when the antenna beam scans through the search volume, a target track is established. The next time the antenna beam passes over this target, the newly collected measurements are used for updating the target track file. As the antenna beam continues its scan, more targets are detected and the measurements are used to form their track files, which are then updated when the beam scans over these targets again.

Since no additional radar resources are required for updating the track files, a large number of targets (more than 1,000) can be simultaneously tracked during search, limited only by the bound on tracking filter throughput and computer memory capacity. However, the track update rate can not be faster than the antenna frame-time (which is typically

in the seconds [1]). Therefore, the TWS mode is only suitable for non-threatening targets such as commercial aircraft. For applications in which the search and track of threats are required (eg., incoming missiles with a demanding track update rate of 0.5 s [3]), the SAT approach should be considered.

In the SAT approach, the antenna scans according to an initial search pattern which is optimised for the initial quiescence condition (i.e., when no targets have been detected) based on the search parameters such as frame-time, priority search sector, etc. If a target is detected, then some of the radar resources are devoted to the tracking of this target. For instance, a revisit beam might be allocated periodically to the target every half a second for track update. The length of the revisit dwell depends on the target size, distance, speed, and the required tracking quality. If another target is detected, then some amount of the radar resources is devoted to the tracking of this second target. In this fashion, the initial search frame-time will become longer and longer for every additional target to be tracked.

Although the track update rate can be made much faster than that in the TWS mode, it is obvious that there is a limited number of targets which can be tracked simultaneously in the SAT mode. For instance, if 5% of the radar resources are allocated for the tracking of each target, then at most 20 targets can be tracked (compared with 1000 in the TWS approach). Radar resources eventually become too few for maintaining effective search for new targets as the number of tracks continues to grow. A radar resource management algorithm is required to ensure an adequate balance between the longest search frame-time and the maximum number of tracks maintained.

In certain applications, it is necessary to implement both TWS and SAT algorithms [1]. For instance, a radar system may have to perform multiple functions, one of which is to search for long range, highly manoeuvring, short-term threats (eg., low altitude cruise missiles). Once a target is detected, it is passed to a target identification process. If the target is identified as a threat, then a track file is formed and updated using the SAT algorithm. Identification of one target may consume only a fraction of a second. However, if there are one hundred potential targets to be identified per scan, the radar will spend many seconds on target identification periodically. Therefore, once the targets are identified as benign, they still have to be continuously tracked; otherwise, those benign targets will be detected repeatedly (in the subsequent scans) and will go through the time-consuming target identification process again. As high precision tracks are not required for those benign targets, their tracks can be maintained using a TWS algorithm.

1.2 Detection Regimes.

In radar detection, the decision on target presence or absence is made by verifying the following two alternative hypotheses [4]:

- H_0 : the received signal contains only noise (i.e., target absent), or
- H_1 : the received signal contains a signal of interest (i.e., target present) and noise.

There are two main approaches to making the decision described above. In the first approach, the decision is made after a fixed observation interval in which the data is

collected. For instance, target presence or absence is determined after the data collected from one dwell has been processed. Here a dwell refers to the transmit and receive of radar pulses at an antenna beam position in the search volume. In the second approach, known as sequential detection, the observation interval is not fixed but varies depending on the data observed. After each observation interval (eg., a dwell), it is decided whether to make a decision based on the available data or to continue collecting more data (eg., make another dwell at the same beam position again for confirmation).

The first approach is often implemented in radar systems equipped with a mechanically scanned antenna, in which the agility of the antenna beam is not in critical demand. This approach leads to a one-step detection procedure where target presence/absence is decided for each dwell.

The theory of sequential detection (i.e., the second approach) has been developed since the 1950s and 1960s [4]. However, as sequential detection requires an agile antenna beam, this approach has only been effectively exploited recently with the deployment of ESA radar systems. A simple case of sequential detection, known as a two-step alert-confirm (or detect-and-confirm) detection procedure, is often implemented.

In the alert-confirm detection process, two antenna dwells are designed for each beam position in the search volume. The second dwell (i.e., confirm revisit) is only made if there are detections (i.e., alerts) declared in the first dwell. In the second dwell, only locations at the alerts are checked. The second dwell is optimised for detecting targets at those alert locations in the search volume. It is reported that there can be between 3.2 dB to 4.4 dB in detection sensitivity improvement compared to the one-step detection [5], [6]. Detection improvement depends on the number of range-Doppler cells to be checked (which determines the false alarm setting), the time available for making confirm revisits (which determines if the revisits are made within the correlation time), and the flexibility of the scan routine controlled by the designed beam scheduling algorithm.

1.3 Beam Scheduling Regimes.

In an electronically scanned radar system like the XPAR-2, the radar can point its beam in any direction almost instantly. This capability calls for the development of new, effective scheduling algorithms, and a variety of them have been proposed in the literature. A survey in [7] reported six different categories of radar resource management algorithms, including adaptive scheduling algorithms and resource aided algorithms. Of particular relevance to the XAPR-2 application is the adaptive update-rate algorithms in which some modification to the traditional uniform tracking revisits is made in order to adapt to the clutter characteristics, target manoeuvring situations, and the required quality of tracking.

For instance, an algorithm which combines maximum expected information gain with maximum target detection probability is presented in [8]. In this algorithm, the search mode and the track mode are considered separately with two optimisation problems to be solved. Another scheduling algorithm known as the Paranoid Tracker that unifies the scheduling of both the search mode and the track mode into one optimisation problem was proposed in [9]. However, in this algorithm the detection of new targets is not optimised.

None of the above radar scheduling algorithms addresses the beam scheduling method for a search mode in which a two-step sequential detection algorithm is implemented.

1.4 Scope of this Work.

Since the TWS detection regime is crucial for any radar systems, in the sense that even if the detection of threats is the primary goal, a TWS procedure is still required for sharing the work-load with the SAT. Therefore, the TWS search regime, a one-step detection algorithm, and a simple beam scheduling algorithm in which the antenna scans with a pre-defined pattern which is never modified during search operation, are considered for the XPAR-2 system. An analysis of the search performance from a radar detection perspective is presented. Waveforms and PRFs which are optimised for detection of targets of interest are designed.

As analysed in Section 1.2, the two-step alert-confirm detection regime can offer considerably improved search sensitivity and is implementable in an ESA radar system. Therefore, the TWS search regime and the alert-confirm detection regime are considered for future research study. To this end, a new beam scheduling algorithm that (i) maximises target detection probability for a given false alarm rate in a two-step detection architecture and, (ii) minimising the frame-time, while (iii) constraining the tracking error to a specified bound, is worthwhile for investigation.

The report is arranged as follows. A brief description of the XPAR-2 system is presented in Section 2, and the XPAR-2 search volume is then defined in Section 3. An overview of the proposed search mode operation is presented in Section 4. The required signal processing and detection algorithms are described in Sections 5 and 6. A procedure for waveform and pulse repetition frequencies (PRFs) selections is summarised in Section 7. Details of the proposed waveforms, PRFs, and detector parameters are presented in Section 8. In Section 9, effects of clutter and phase noise on detection performance are discussed. Search mode operation when some of the active elements of the antenna array are not available is considered in Section 10. Proposed future work is presented in Section 11, and detailed computations are shown in the appendix.

2 Description of the XPAR-2 System.

A brief description of the XPAR-2 system is presented in this section, while more details can be found in the reference therein. The XPAR-2 is a ground-based radar system developed at DSTO and is located at the Sensor Trials Facility (STF) near the Edinburgh airfield. The system consists of an L-band active aperture antenna, multiple IF receivers, a high speed recording device capable of capturing large volumes of data from the receivers and signal processing intermediate stages, a multi-mode controller, and a graphical user interface (GUI) operator console.

The antenna array consists of 10×10 array elements, 8×8 of which are available for beamforming with potential true time-delay beam steering capability. The array is arranged in eight vertical columns which operate as eight channels driven by eight transmitters. For each column, a Sum receiver and a Difference receiver are provided. Linear slant

polarisation is employed. Full electronic beamforming in azimuth can be performed (with some limited degree of beamforming in elevation) [11].

3 Search Volume.

The geographic coverage of XPAR-2 radar is shown in Fig.1. Adelaide, the capital city of South Australia, is located between the Gulf St Vincent and the Mount Lofty Ranges, stretching 11 NM from the west coast to the east foothills.

The radar is at location O (i.e., at the STF) which is 13 NM from the Adelaide central business district (CBD). For bearing description, as in Google Earth [10], the south-to-north direction is at 0 degree, with positive increment in clockwise rotation. The antenna boresight aligns in the direction OC at 197 degrees [11], pointing toward Adelaide airport which is at point A, approximately 15 NM from the radar. The azimuth search sector is limited by OB at 245 degrees (pointing toward Outer Harbor) and OD at 156 degrees (pointing toward Parafield airport which is at point P, approximately 5 NM from the radar). The foothill border is marked by the line MN which aligns in the south-west to north-east direction.

The targets of interest are small aircraft with radar cross-section (RCS) between 1 m² to 10 m² at ranges up to 7 NM, and large commercial aircraft with RCS of approximately 100 m² at ranges between 15 NM to 20 NM. The maximum target velocity is Mach-1 (approximately 340 m/s), while the maximum target acceleration is 2*g*. The search for new targets is performed in two dimensions (2-D), i.e., azimuth search only. In this 2-D search operation, the radar is designed to cover a volume specified by an azimuth sector $\Theta_{max} = 90$ degrees, a maximum range $R_{max} = 20$ NM, and an elevation sector covering from the horizon to θ_2 (see Fig.2). The beam is shaped to give a detection contour at a constant altitude from elevation angle θ_1 to θ_2 .

3.1 Elevation Coverage of an Antenna Beam.

The antenna beam is formed with a cosecant-squared pattern. As shown in Fig.2, the long-range lobe covers elevation angles from the horizon to θ_1 , while the broaden main-lobe upper edge extends the elevation coverage to angle θ_2 . For this application, $\theta_1 = 13$ degrees, $\theta_2 = 45$ degrees [12], and maximum altitude $h_a = 10,000$ m. Assume that the antenna gain is $G(\theta)$, $\theta \in [0, \theta_1]$, the following antenna gain pattern provides a detection contour at a constant altitude for elevation angle $\theta \in (\theta_1, \theta_2)$ [6]:

$$G(\theta) = G(\theta_1) \frac{\csc^2(\theta)}{\csc^2(\theta_1)}, \quad \theta_1 < \theta < \theta_2 \quad (1)$$

3.2 Azimuth Coverage of an Antenna Beam.

In antenna co-ordinates, by definition the beam angle at boresight is 0 degree; a negative beam direction denotes a beam position which is on the left of boresight, while a positive

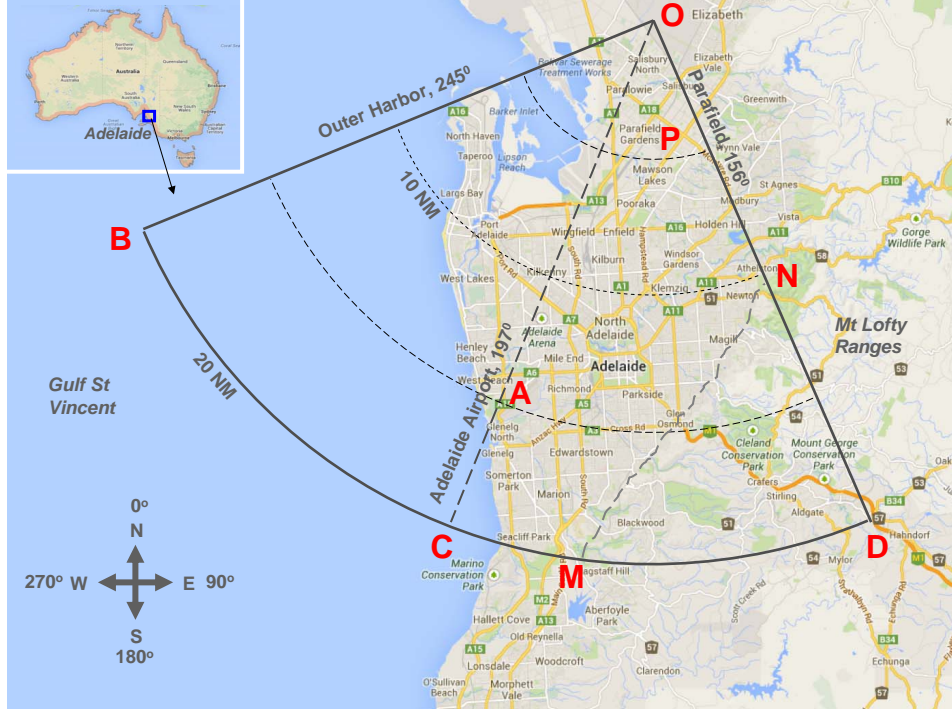


Figure 1: Geographic coverage of XPAR-2 radar

beam direction denotes a beam position on the right of boresight. Azimuth beamforming is performed with the following Chebyscheff weights (computation method can be found in [13]):

$$[0.2622, 0.5187, 0.8120, 1, 1, 0.8120, 0.5187, 0.2622], \quad (2)$$

which gives approximately -30 dB side-lobes. Five azimuth beams are formed as shown in Fig.3(a), in which adjacent beam intersections occur at the 3 dB beamwidth points. The total azimuth coverage is approximately 90 degrees. To alleviate the detection loss for targets that are in the vicinity of those 3 dB beam overlaps, another four beams are formed and shown in Fig.3(b), in which the peak gain of each beam occur at the 3 dB beamwidth points of the previous five beams. The total nine beam directions and their corresponding 3 dB beamwidths are listed in Table 1.

Table 1: Beam direction θ and 3 dB beamwidth Θ_{3dB} .

Direction label	1	2	3	4	5	6	7	8	9
θ , degrees	-32.8	-16.4	0	16.4	32.8	-24.75	-8.25	8.25	24.75
Θ_{3dB} , degrees	20.2	17.2	16.4	17.2	20.2	18.4	16.7	18.4	16.7

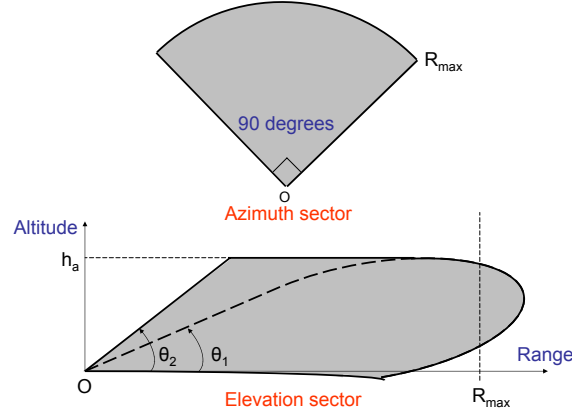


Figure 2: XPAR-2 search volume.

4 Search Mode Operation.

The search for new targets is described as follows.

4.1 Search Operation.

The antenna performs azimuth scan by stepping its beam over each of the nine azimuth positions in the following pattern:

$$a_1 - a_2 - a_3 - a_4 - a_5 - a_6 - a_7 - a_8 - a_9 \quad (3)$$

where the letter a is the abbreviation for azimuth, and the numbers denote the nine azimuth directions summarised in Table 1.

The antenna beams are scheduled for transmit-receive at the following discrete time slots determined by the radar controller:

$$t_0, t_1, \dots, t_k, t_{k+1}, \dots \quad (4)$$

The time interval $e_k = [t_k, t_{k+1}]$ is referred to as a dwell. The frame-time is defined as the time it takes the antenna to scan its dwells over the search volume.

In the beam schedule list, there are nine azimuth beam positions as shown in (3) which form the schedule for one frame-time ahead. The schedule of a dwell at time t_k is specified by the set $\{d_k(a_k), W_k\}$, i.e., a beam direction $a_k \in \{a_1, a_2, \dots, a_9\}$, the corresponding dwell time d_k , and the set W_k of waveforms and PRFs in use. Those three parameters are determined by the search algorithm.

The beam scheduling is summarised in Fig.4 and explained as follows:

1. Assume that the current epoch is e_k , and the dwell to be executed is $\{d_k(a_k), W_k\}$. The time labels are:

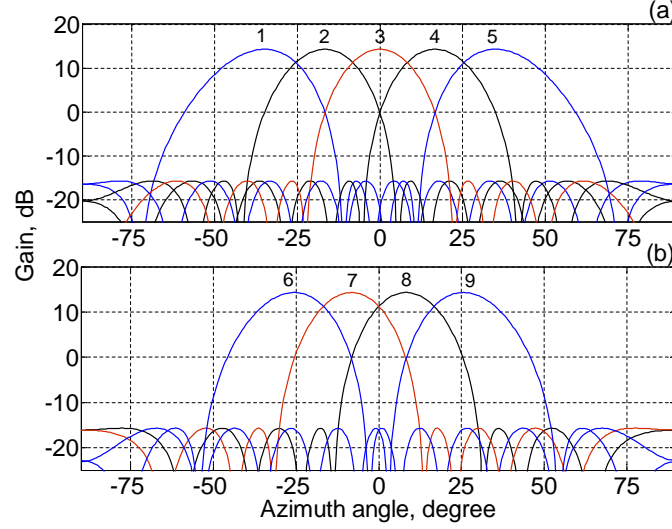


Figure 3: Nine azimuth beams per scan for search mode operation.

- current time: $t = t_k$,
 - the previous dwell finished at time $t^- = t_{k-1} + d_{k-1}$, which is also the start time for the processing of previously collected data,
 - the current dwell will finish at time $t^+ = t_k + d_k$,
2. During the time interval $[t, t^+]$, there are two parallel operations: performing transmit-receive of radar pulses and processing of previously collected data (denoted as data received up to time t^-).
 3. Once the transmit-receive has been finished at an azimuth position, that azimuth position is re-scheduled to the lowest priority location in the schedule list. For instance, assume that the current schedule list is as in (3), in which the highest priority is the azimuth position at the left end (i.e., a_1) while the lowest priority is the azimuth position at the right end (i.e., a_9). After the transmit-receive has been finished at azimuth a_1 , the schedule list is up-dated as:

$$a_2 - a_3 - a_4 - a_5 - a_6 - a_7 - a_8 - a_9 - a_1 \quad (5)$$
 4. The azimuth position with the highest priority in the schedule list, which is a_2 in list (5), is selected for the next epoch. Communication with the radar scheduler is then established for the next transmit-receive.
 5. While waiting for the next dwell, the data collected up to time t^+ are processed.
 6. Assume that time t_{k+1} is granted for the next dwell, the time labels are updated to:
 - current time: $t = t_{k+1}$,

- previous data collected time finished at: $t^- = t_k + d_k$,
- next data collected time will finish at: $t^+ = t_{k+1} + d_{k+1}$,

The process continues by repeating from step 2 of Fig.4.

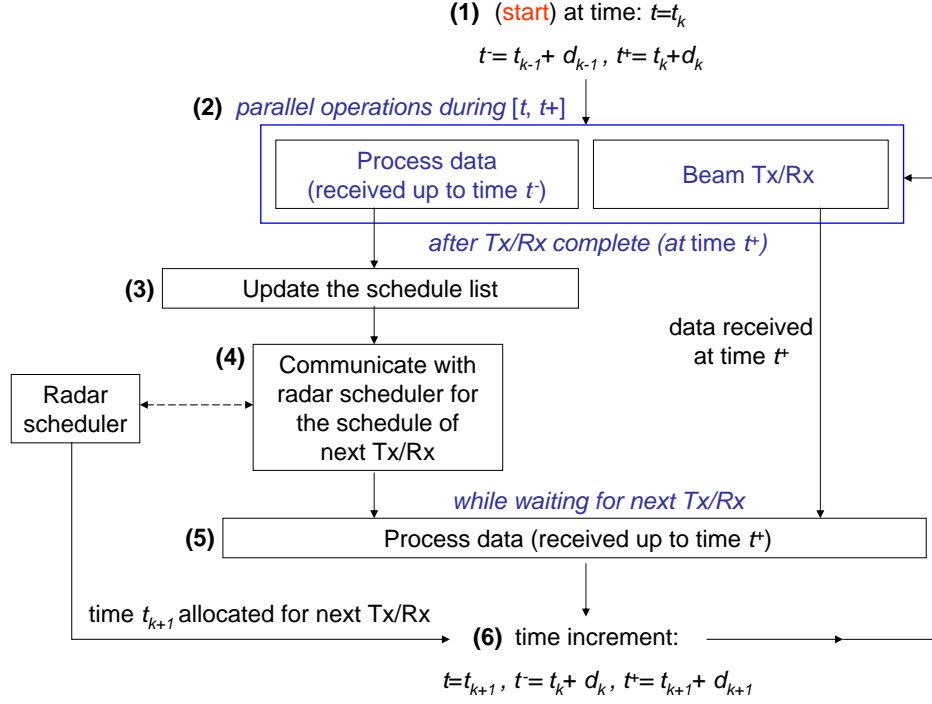


Figure 4: Overview of search mode operation.

4.2 Track-while-Scan Processing.

In this section, the signal processing steps of a track-while-scan search is described. The corresponding data processing steps (such as the data association algorithm and tracking method) belong to the tracker design and therefore are not in the scope of this report.

The signal processing in step (2) of Fig.4 is explained further in this section. Following the transmit-receive at each azimuth position, radar returns are processed by the Sum channel, the Difference channel, and the Guard channel as shown in Fig.5. Those receiving channels are formed via beamforming. Signal detection is then performed in the Sum channel.

- If no signal is detected (i.e., no hits), then the azimuth scan continues;
- Otherwise (i.e., with hits), the signals detected in the Sum channel are then compared with those at the same locations in the Guard channel in order to verify that the

hits are not from the antenna side-lobes. If side-lobe hits are identified, the azimuth scan continues; otherwise (i.e., main-lobe hits are found), the hits are resolved for finer angle measurements using data from the Difference channel.

- Measurements of main-lobe hits, which include range, velocity, azimuth-elevation angles, and uncertainty, are then passed to the tracker, and the azimuth scan continues.

4.3 Guard Channel Operation.

Operation of the Guard channel, also known as side-lobe blanking [14], is explained as follows. Radar echoes may come from air targets as well as from unwanted ground targets (eg., trucks, high-speed vehicles, etc). While echoes from the air targets fall within the Sum channel main-lobe, echoes from the ground targets may return to the Sum channel side-lobes. Ground targets may have very large RCS with Doppler frequencies within the Doppler filter pass-band. Therefore, ground targets may be detected to the same extent like air targets. To prevent those unwanted ground targets to be misinterpreted as air targets, a Guard channel is employed.

From a beam-forming point-of-view, the Guard channel can be formed as a weighted incoherent summation of the array elements in the Sum channel [15]. The weights can be uniform to give a uniform gain over all azimuth angles. As reported in [16], the gain of the Guard pattern should at least 15 dB, and can be as low as 40 dB, below that of the Sum main-lobe peak. Therefore, the Guard pattern gain is not a critical design parameter with narrow efficiency margin. In this application, as the Sum side-lobes are in the range of 30 dB below the main-lobe peak [17], a Guard level of 20 dB below the Sum main-lobe peak is selected.

An ideal Guard pattern formed as the incoherent summation of eight array elements is shown in Fig.6. The width of the Guard pattern is sufficiently wide to cover the whole region illuminated by the Sum side-lobes, while the gain of the Guard pattern is larger than any of the Sum side-lobes. Any target that falls within the Sum channel side-lobes will produce a stronger return in the Guard channel. Therefore, by comparing the output of the Sum channel to that of the Guard channel, a target in the main-lobe of the Sum channel can be deduced.

4.4 Measurements.

Once a main-lobe hit is confirmed, measurements of target range, velocity, and azimuth (and also elevation with some degree of restriction) are then performed.

4.4.1 Measurement of Range and Velocity.

Target range and velocity are measured using a centroiding algorithm [1], p693. Assume that a sequence of hits of amplitudes $x[l]$ are found at consecutive ranges (or velocities)

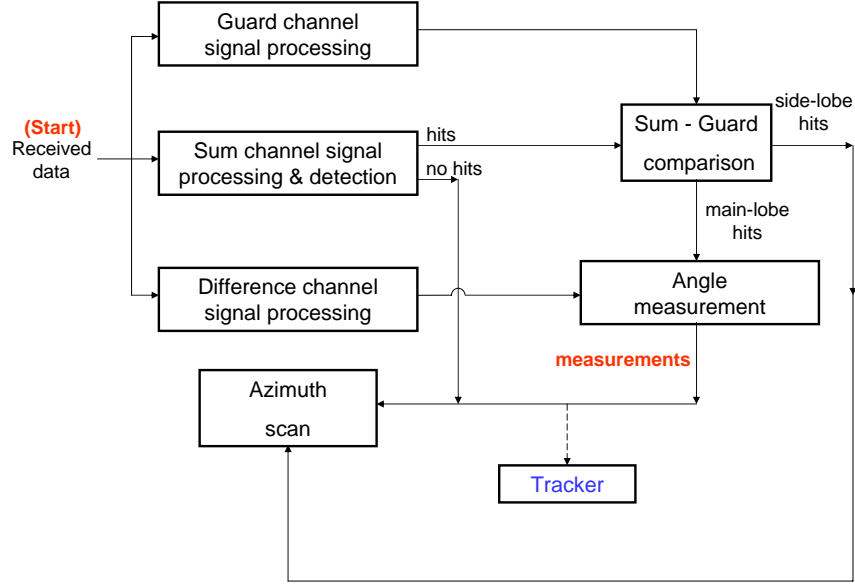


Figure 5: Overview of track-while-scan signal processing.

from range (or velocity) L_1 to range (or velocity) L_2 , the resulting measurement is the centroid C_x over the region $l \in [L_1, L_2]$ of the hit sequence $x[l]$:

$$C_x = \frac{\sum_{l=L_1}^{L_2} lx[l]}{\sum_{l=L_1}^{L_2} x[l]} \quad (6)$$

4.4.2 Measurement of Azimuth Angle.

As the 3 dB azimuth beamwidth of each beam is large (at least 16.4 degrees as shown in Table 1), a finer detail of the target whereabouts can be obtained using the following monopulse technique [18], p.308. The angle error with respect to boresight is:

$$\delta a = \text{Re} \left(k \frac{\Delta \Sigma^*}{\Sigma \Sigma^*} \right) \quad (7)$$

where Δ and Σ are the (complex) Different and Sum channel outputs, respectively; k is a constant; 'Re' denotes the real part; and the asterisk superscript denotes the complex conjugate.

Based on (7), angle measurement is performed as follows:

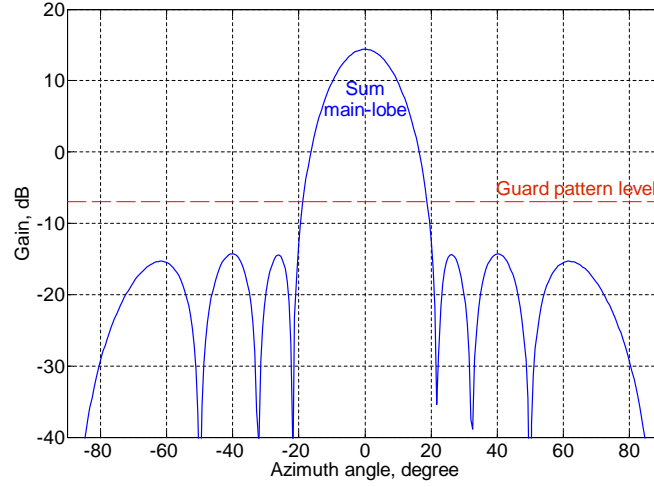


Figure 6: Concept of a guard channel.

- At each of the nine beam positions shown in Fig.3, using the formed beam pattern Δ and Σ , a calibration curve is constructed as the ratio $\text{Re}(\Delta\Sigma^*)/(\Sigma\Sigma^*)$. The constant k in (7) is estimated as the slope of this calibration curve. The nine constants are then stored in a look-up table.
- For measured values of Δ and Σ , the angle error is then the product of the corresponding constant k in the look-up table and the measured ratio $\text{Re}(\Delta\Sigma^*)/(\Sigma\Sigma^*)$.

Similarly, elevation angle measurement can be performed using the same monopulse technique described above.

4.4.3 Measurement Uncertainty.

For a parameter α , which can be either range, velocity, or angle, the variance σ^2 of the measured (or estimated) value $\hat{\alpha}$ has the following relationship with the target SNR [1], p689:

$$\sigma^2 = \frac{\text{Constant}}{\text{SNR}} \quad (8)$$

The constant in (8) can be found by establishing a Cramer-Rao lower-bound which is the minimum achievable variance of an unbiased estimator of the parameter α . In principle, measurement precision improves with finer resolution and higher target SNR as follows.

- Let ΔR be the range resolution. The range precision is then [1]:

$$\sigma_R \geq \frac{\Delta R}{\sqrt{\text{SNR}}} \quad (9)$$

- Let ΔF be the frequency resolution. The Doppler frequency precision in Hz is [1]:

$$\sigma_F \geq \frac{\sqrt{3}}{\pi} \frac{\Delta F}{\sqrt{SNR}} \quad (10)$$

- Let $\Delta\Theta$ be the 3 dB azimuth beamwidth. The angle precision is [6]:

$$\sigma_\Theta \geq \frac{\Delta\Theta}{1.61\sqrt{SNR}} \quad (11)$$

Note that in practice, in addition to the above SNR-related error, there will be other errors that are more difficult to quantify (for instance, error in calibration).

5 Signal Processing.

At each beam position, the radar transmits N bursts of pulses using N different PRFs, N different waveforms, and N different carrier frequencies as shown in Fig.7. The N PRFs and N waveforms are selected such that range and velocity ambiguities can be resolved.

On receive, the returned pulses in each of these N bursts are coherently processed to give a range-Doppler map (RD-map). Target detection is then performed in each of the N RD-maps via two thresholding tests, i.e., constant false alarm rate (CFAR) test and binary detection test. The CFAR test detects targets on a cell-by-cell basis using an adaptive threshold computed at each cell in an RD-map. Any entry in an RD-map that exceeds the adaptive threshold is denoted as a CFAR hit. CFAR hits are then integrated (i.e., counted) over N RD-maps (at the corresponding range-Doppler locations) using a binary integrator. If there are at least M CFAR hits out of N RD-maps (i.e., second thresholding test using M -of- N combination), a target is declared.

The reason for this signal processing and detection architecture is explained as follows. When the radar transmits a train of pulses, there are four methods for processing the information contained in the received pulse train. These methods are listed in order of declining processing efficiency (in terms of achieved signal-to-noise ratio (SNR)) as follows [6], p.47:

- Coherent processing
- Noncoherent processing
- Binary integration
- Cumulative detection

In order to take advantage of the most effective coherent processing, each of the N bursts are coherently transmitted. On receive, radar returns are processed using discrete Fourier transform (DFT). Due to possible range and Doppler ambiguities, one coherently processed burst is often not sufficient for taking target measurements. This is why $N > 2$ bursts of coherent pulses are employed. The next signal processing method to be considered is the noncoherent processing which can be performed by adding the N samples

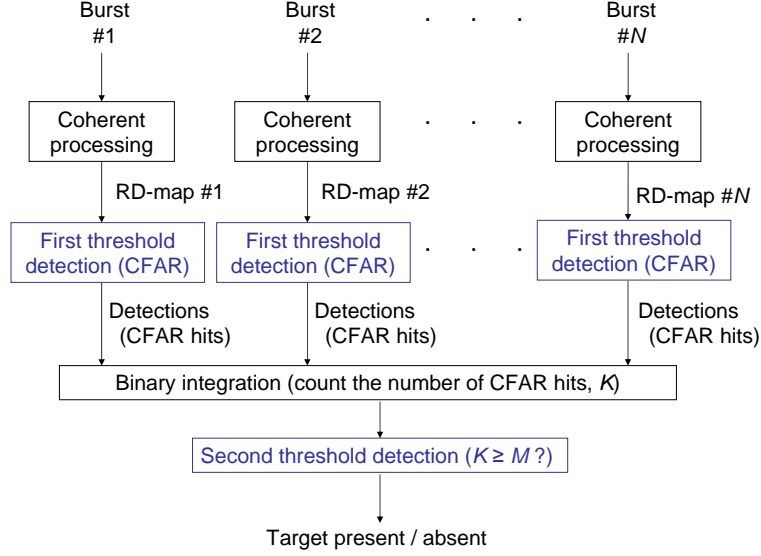


Figure 7: Signal processing and detection at each beam position.

(at the same location) over N RD-maps. However, again due to range and Doppler ambiguities, the same range-Doppler location in a different RD-map may contain a return from a different true range and a different true Doppler frequency. Noncoherent processing method then is impossible without the adjustment of the (unknown) target range and Doppler frequency prior to noncoherent integration. This is why binary integration is employed. Binary integration allows the resolving of possible range-Doppler ambiguities while improving target SNR.

A detailed analysis of the Doppler spectrum is described in Fig.8 [18]. Input of this signal processing step is a 2-D matrix of complex entries (I and Q data). Each column of the matrix, known as fast time data, consists of successive samples of the return from a single pulse. These samples are called range samples (or range bins) as they are collected at sampling interval equal to the compressed pulse-width which defines the range resolution. Each row of the matrix, known as slow time data, consists of samples at the same range bin over successive pulses. These samples are called Doppler samples (or Doppler bins) as they are collected at sampling interval equal to the pulse repetition interval (PRI) over the length of the CPI which defines the Doppler resolution.

DFT input is a discrete-time sequence of complex (I and Q) samples from the same range bin with sampling interval PRI. For length N_p input sequence $x[n]$, $n = 1, 2, \dots, N_p$, the DFT output is computed as follows [18]:

$$X[k] = \sum_{n=0}^{N_p-1} x[n]w[n] \exp(-j2\pi nk/N_p), \quad k = 1, 2, \dots, N_p$$

$$w[n] = 0.54 - 0.46 \cos\left(\frac{2\pi n}{N_p - 1}\right) \quad (12)$$

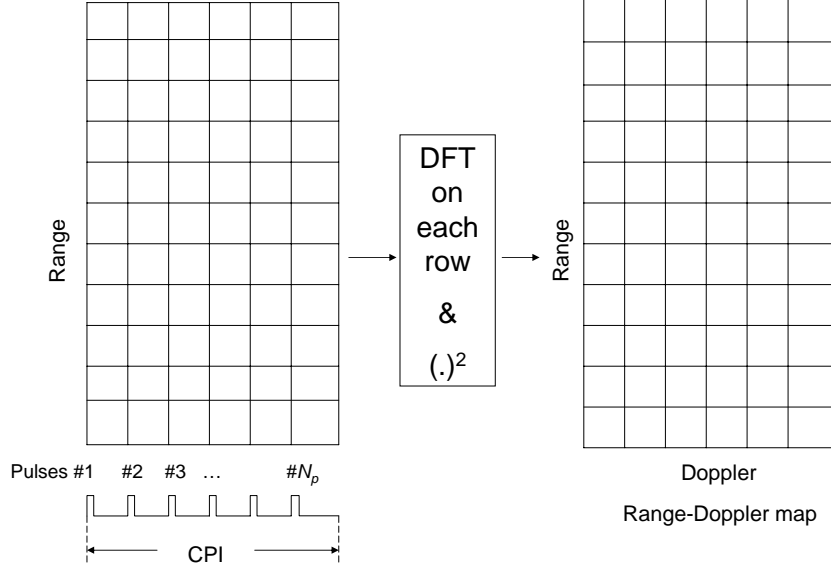


Figure 8: Signal Processing of one CPI.

where $w[n]$, $n = 0, 1, \dots, N_p - 1$, is the Hamming window function for reducing the DFT side-lobes. For Hamming window, the first side-lobe is -41 dB (compared with -13.46 dB of the case without windowing, $w[n] = 1$), while the main-lobe width is twice that of the case without windowing [19].

Output from the DFT processing is a range-Doppler map which is a 2-D matrix, each column of which forms a range profile at a Doppler bin; while each row of which forms a Doppler profile at a range bin. In the next section, target detection is addressed.

6 CFAR Detection and Binary Detection.

At each beam position, two thresholding tests are performed at each cell of an RD-map, namely the CFAR test and the binary detection M -of- N test, and target detection requires that both tests are passed. In this section, the false alarm rates and target detection probabilities of these two tests are computed. Calculation of target SNR using the radar equation is also addressed.

The following assumptions are made:

- Assumption 1. Target radar cross-section (RCS) fluctuates according to Swerling-1 model, and the interference is Rayleigh distributed.
- Assumption 2. Target detection is performed on an independently and identically distributed (IID) background.

6.1 Computation of Target Signal-to-Noise Ratio.

For a given range R , target signal-to-noise ratio (SNR) is computed by the following radar equation [6], p.12:

$$SNR = \frac{P_{av} t_f G_t G_r \lambda^2 \sigma}{(4\pi)^3 k T L R^4} \quad (13)$$

where the average transmission power is $P_{av} = P_t \times D_u$ (P_t is the peak transmission power, D_u is the duty cycle); t_f is the CPI which is selected such that a target manoeuvring at $2g$ still stays in one velocity resolution cell (see Appendix A for details); other parameters are described in Table 2.

Details of the radar losses are shown in Table 3 and are quantified as follows.

- Transmit and receive losses: there is a transmit loss between the radar transmitter and the antenna input port. There is also a receive loss between the antenna output port and the receiver front end. Those losses are referred to as plumbing loss and are typically between 1 and 2 dB [19], p57.
- Atmospheric loss: atmospheric attenuation depends on radar carrier frequency as well as target range and elevation angle. For L-band radar, at range less than 50 km and elevation angle less than 10 degrees, atmospheric attenuation is less than 0.5 dB [6], p270.
- Beam shape loss: if the target is not on the antenna boresight axis, then there is a loss in target SNR since the antenna gain in the target direction is not maximum as assumed in the radar equation. This loss is less than 3 dB if the target is still within the radar 3 dB beamwidth.
- Array scan loss: this loss is due to a reduction in the array effective aperture as the antenna is electronically steered away from the array boresight. At azimuth scan angle θ , such loss can be approximated as $\cos(\theta)^{2.5}$ [19], p457. With $\theta = 32.8$ degrees (see Table 1, beam 5), the associated scan loss is around 3 dB.
- Signal processing loss: this includes filter mismatching loss (≈ 1 dB), CFAR detection loss (≈ 1.2 dB), Doppler filter straddle (≈ 2.5 dB), and range gate straddle (≈ 2.5 dB).
- Other losses: this may include losses due to antenna calibration error, antenna efficiency, etc.

6.2 CA-CFAR Detection.

A common routine test in any detection system is to compare the received signal level with a pre-defined threshold value. In this application, the first detection threshold is set to give a constant false alarm rate (CFAR). The most basic form of CFAR processor, i.e., the cell-averaging CFAR (CA-CFAR), is implemented since it is optimal under Assumptions 1 and 2 in the sense that for a specified false alarm rate, the highest target detection probability is achieved [20].

Table 2: Radar and target parameters.

Radar frequency, L-band, GHz ...	1.3
Radar wavelength, λ , m ...	0.2308
Transmission peak power, P_t , 8×250 , W ...	2000
Duty cycle, D_u ...	0.1
Coherent processing interval, t_f , s ...	0.076
Transmission gain, G_t , dB ...	19
Receiver gain, G_r , dB ...	18.3
Boltzmann constant, k , JK^{-1} , ...	1.38×10^{-23}
Effective temperature, T , K ...	750
Radar loss, L , dB ...	18.6
Target RCS, σ (typical values), m^2 ...	1, 10, 100
Maximum target velocity (Mach-1), m/s ...	340
Maximum target acceleration ...	$2g$

Table 3: Radar losses in dB.

Transmit and receive losses ...	2
Atmospheric loss ...	0.5
Beam shape loss ...	3
Array scan loss ...	3
Signal processing loss ...	7.2
Other losses ...	3
Total loss L ...	18.7

6.2.1 Description of the CA-CFAR Detector.

An implementation of the CA-CFAR detector is shown in Fig.9. Input to the detector is the squared-law detected entries of an RD-map. The following procedure is performed on a cell-by-cell basis.

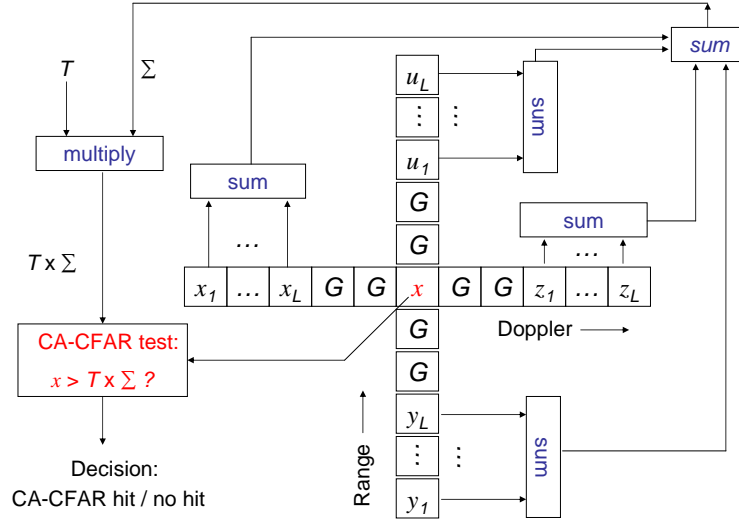


Figure 9: Description of the CA-CFAR Detector.

The signal level x in the test cell (where a decision on target presence or absence has to be made) is compared to a threshold. A CA-CFAR hit is declared at this range-Doppler cell if x exceeds this threshold, which is computed by multiplying the interference estimate with a constant T , the value of which is determined by the required false alarm rate. The interference is estimated using the surrounding cells (which are termed reference cells): $x_1, x_2, \dots, x_L, z_1, z_2, \dots, z_L$ (in the Doppler dimension), and $y_1, y_2, \dots, y_L, u_1, u_2, \dots, u_L$ (in the range dimension). The estimate is simply the summation of these $4L$ reference samples. Two immediate neighbours (known as guard cells, denoted as G in Fig.9) on each side of the test cell are excluded from the estimation to prevent possible signal spillover from the test cell. The spillover may happen if the target signal is too strong and/or the target straddles between two consecutive resolution cells.

Near the edges of the RD-map, one or two branches of the CA-CFAR detector may not have the full length of L reference cells. In these situations, more cells in the opposite branches are employed so that the total number of reference cells remains $4L$.

6.2.2 CA-CFAR False Alarm Rate and Detection Probability.

For a specified false alarm rate F_{CA} , the threshold multiplier T is given by:

$$T = (F_{CA})^{-1/L_{CA}} - 1 \quad (14)$$

where $L_{CA} = 4L$. For a Swerling-1 target, the detection probability is then [20]:

$$P_{CA} = [1 + T/(1 + SNR)]^{-L_{CA}} \quad (15)$$

where SNR is the signal-to-noise ratio of the target. For performance comparison, the detection probability of the optimal detector (in which the number of reference cells $4L = \infty$) is:

$$P_{opt} = (F_{CA})^{1/(1+SNR)} \quad (16)$$

The number of reference cells is selected as follows. Detection probabilities of a Swerling-1 target at false alarm rate $F_{CA} = 10^{-6}$ for the optimal detector and CA-CFAR detector with window length $L_{CA} = 16, 24$ and 32 are shown in Fig.10. Compared with the optimal detector at 50% detection, CA-CFAR has a detection loss (defined as the additional target SNR required to achieve the same probability of detection given by the optimal detector) of approximately 2 dB, 1.3 dB, and 1 dB when using window length $L_{CA} = 16, 24$ and 32 , respectively. The CFAR window length is selected such that the CFAR loss is minimised while the window length is not too long so that the interference estimate still statistically represents the interference in the test cell. For this reason, the CFAR window length $L_{CA} = 24$ is selected, giving a CFAR loss of 1.2 dB.

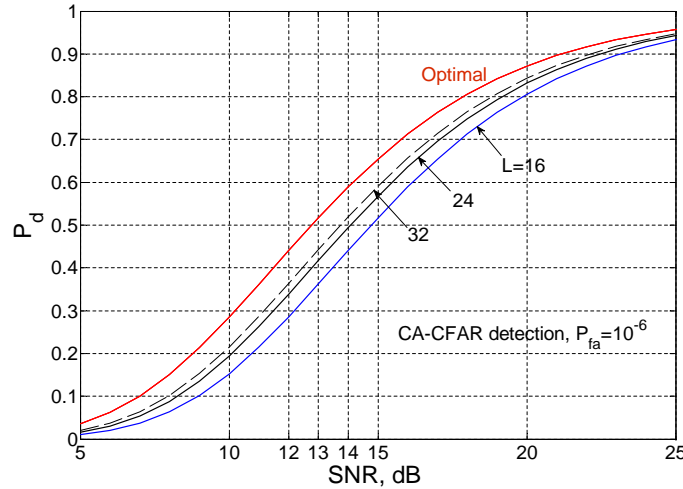


Figure 10: Detection probability for selection of CFAR window length.

6.3 M -of- N Binary Detection.

After CA-CFAR detection, the CFAR hits obtained from N RD-maps are counted. If there are at least M hits at the same location in the RD-map (i.e., M -of- N decision rule),

a target is declared. The false alarm probability P_{fa} and detection probability P_D of the binary detector is given by the following binary distribution [4]:

$$P_{fa} = \sum_{K=M}^N C_N^K (F_{CA})^K [1 - F_{CA}]^{N-K} \quad (17)$$

$$P_D = \sum_{K=M}^N C_N^K (P_{CA})^K [1 - P_{CA}]^{N-K} \quad (18)$$

$$C_N^K = \frac{N!}{K!(N-K)!} \quad (19)$$

where F_{CA} and P_{CA} are the false alarm and target detection probabilities of the CA-CFAR detectors, respectively.

The M -of- N binary decision rule is selected as follows.

- In order to resolve the range and velocity ambiguities of a target, three PRFs are often required [18]. An initial choice of the binary detector is $M = 3$ and $N = 3$ (i.e., 3-of-3 decision). For other choices of N , the best detection curves for $N = 4$ to 10 are shown in Fig.11. These curves are computed using equations (18) and (15), where target SNR is calculated using equation (13) in which the coherent processing time $t_f = t_{max}/N$, where $t_{max} = 0.076$ s is the maximum CPI. For this calculation, the frame time does not increase as N increases since the same coherent processing time is employed.
- From Fig.11, another choice for M -of- N rule is the 3-of-8, since it offers nearly the best target detection for detection probability above 90% while maintaining its detection performance in the region below 90% within the average of other cases. In addition, $M = 3$ hits in 3 different PRFs are sufficient for range and velocity ambiguity resolving (compared with, for instance, the 2-of-7 or 2-of-6 rules with only 2 hits in 2 different PRFs).
- When the target is blind to one of the PRFs in a dwell, the 3-of-8 rule (i.e., $N = 8$) is also more robust compared with the case where $N = 5, 6$, or 7. For instance, consider the case when the target is blind to one PRF. For the 3-of-8 rule, the dwell time (available for target detection) reduces by 12.5% (i.e., $1/8$); whereas for the case $N = 5, 6$, or 7, the dwell time reduces by 20%, 16.7%, or 14.3%, respectively (i.e., corresponding to $1/5, 1/6$, or $1/7$).

In summary, the 3-of-8 binary integration rule is selected for implementation.

7 Waveform & PRF Design.

The waveforms and PRFs are selected based on the following guidelines:

- In order to detect targets with a maximum acceleration of $2g$, the longest coherent processing interval (CPI) is 0.076 s (see Appendix A).

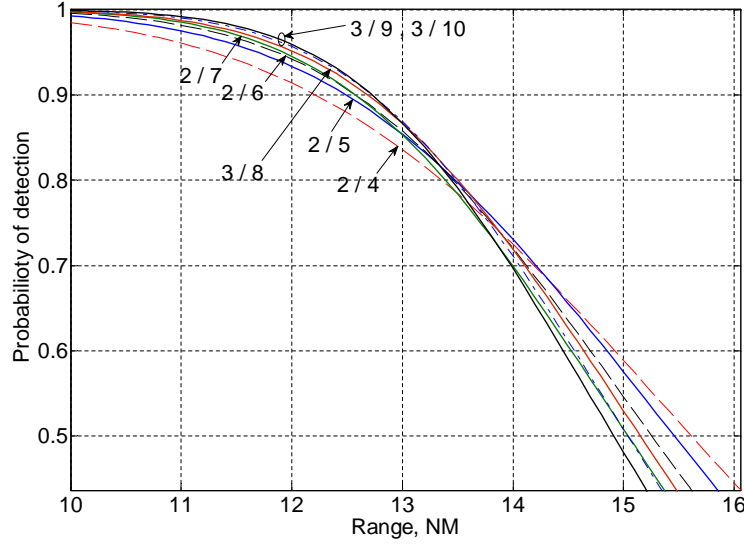


Figure 11: *M-of-N selection.*

- The carrier frequencies of N CPIs corresponding to N bursts of Fig.7 should be spaced by at least f_{corr} but still within the radar operating band, where f_{corr} is the target correlation frequency. With such carrier frequency spacing, independent samples can be obtained across those N bursts, which in turn leads to an improved binary integration gain and a reduced target fluctuation loss [6].
- The PRF in each CPI should be selected such that the range and velocity blind zones are minimised in the regions of interest.
- The time of each dwell should be long enough to give at least 90% detection probability for targets of interest within the range of interest.
- The duty cycle is limited to 10%, since the originally designed transmit-receive modules support 10% duty at full power.

7.1 Waveform Design.

For waveform design, three parameters are to be selected: (i) the type of waveform in use, eg., linear frequency modulation (LFM), Barker coded, etc.; (ii) the uncompressed pulse-width, i.e., the time length of the waveform; and (iii) the bandwidth of the waveform.

Since detection is the primary goal, LFM waveforms are selected. The reason is that LFM waveforms are relatively insensitive to signal degradation at the output of the pulse

compression filter due to Doppler shifted signals [18], p181. For a given range resolution ΔR , the bandwidth of the LFM waveform is:

$$B = \frac{c}{2\Delta R} \quad (20)$$

The compressed pulse width is:

$$\tau_c = \frac{1}{B} \quad (21)$$

For a given PRF and a duty cycle D_u , the uncompressed pulse width is:

$$\tau_u = \frac{D_u}{PRF} \quad (22)$$

The pulse compression ratio is then:

$$C_r = \frac{\tau_u}{\tau_c} = \frac{D_u}{PRF} B \quad (23)$$

7.2 PRF Selection.

There are two main methods of PRF operation for resolving range and velocity ambiguities: the M -of- N method and the major-minor method [18]. The M -of- N method has been implemented in mechanically scanned antenna radars in which a one-step detection algorithm is employed. At each dwell, N PRFs are used. If hits are found in at least M PRFs, then a target is declared. Those M PRFs are then used for resolving range and velocity ambiguities. For the major-minor technique, range-velocity ambiguities are resolved in two steps. Usually in the first step, 3 major PRFs are employed. Once a hit is found in one of the major PRFs, the search proceeds to the second step in which another two minor PRFs are then used for range-velocity ambiguity resolving. This method can be effectively exploited in ESA radars in which a two-step detection algorithm is implemented.

As analysed in Section 6.3, the 3-of-8 PRF operation is suggested for XPAR-2 application. If hits are found in at least 3 out of 8 PRFs, a target is declared and those 3 PRFs are adequate for resolving range and velocity ambiguities. For each PRF, calculation of the following parameters are required: the width of the range blind-zone, the width of the velocity blind-velocity, the unambiguous range, and the unambiguous velocity.

- Range blind-zone width: from (22), the width of the range blind-zone is then:

$$\Delta_r = c\tau_u/2 = \frac{cD_u}{2PRF} \quad (24)$$

- Velocity blind-zone width: the width of the velocity blind-zone, i.e., the band lost to effective target detection is [6], p.241:

$$\Delta_v = \Delta_c + \frac{2v_b}{n_c} \quad (25)$$

where:

- Δ_c is the width of the stop-band which can be estimated from the clutter velocity spread σ_v . For land clutter with vegetation in windy conditions, the velocity spectrum is narrow and is modeled as Gaussian with variance $\sigma_v < 0.5$ m/s [6], p116. A 40 dB clutter rejection requires a stop-band $\Delta_c \approx 6\sigma_v$ (3 m/s).
- the blind speed v_b and the number of pulses n_c are given by [6], p220:

$$\begin{aligned} v_b &= \lambda PRF/2 \\ n_c &= t_f PRF \end{aligned} \tag{26}$$

where λ is the radar wavelength and t_f is the coherent processing time.

The width of the velocity blind zone is then:

$$\Delta_v = \Delta_c + \frac{\lambda}{t_f} \tag{27}$$

- Unambiguous range and velocity: the PRF is related to the maximum unambiguous velocity V_u according to [6]:

$$PRF = 4 \times V_u / \lambda \tag{28}$$

The corresponding unambiguous range, R_u , is then [6], p317:

$$R_u = \frac{c(1 - D_u)}{2 \times PRF} \tag{29}$$

where c is the speed of light; and D_u is the duty cycle.

Given the duty cycle $D_u = 0.1$, pulse repetition frequencies versus maximum unambiguous range and maximum unambiguous velocity are shown in Fig.12(a) and Fig.12(b), respectively. For a specified maximum unambiguous velocity of Mach-1 (340 m/s) and maximum unambiguous range of 20 NM, it is clear that one PRF is not sufficient for achieving both range and velocity unambiguity. For instance, to be unambiguous in velocity ($V_u \approx \text{Mach-1}$), the PRF should be around 6 kHz or higher (Fig.12(b)), whereas to be unambiguous in range ($R_u \geq 15$ NM), the PRF should be around 4.5 kHz or smaller. Therefore, at least two PRFs are required for target detection, usually three PRFs are employed for completely resolving range-Doppler ambiguities.

7.3 Carrier Frequency Selection.

The correlation frequency of the target is p.67 [6]:

$$f_{corr} = \frac{c}{2L_r} \tag{30}$$

where c is the speed of light and L_r is the radial length of the target. For aircraft of body lengths between 10 to 40 metres, f_{corr} is between 15 MHz to 3.75 MHz. The carrier frequencies then should be spaced at least 3.75 MHz apart (and best at 15 MHz apart).

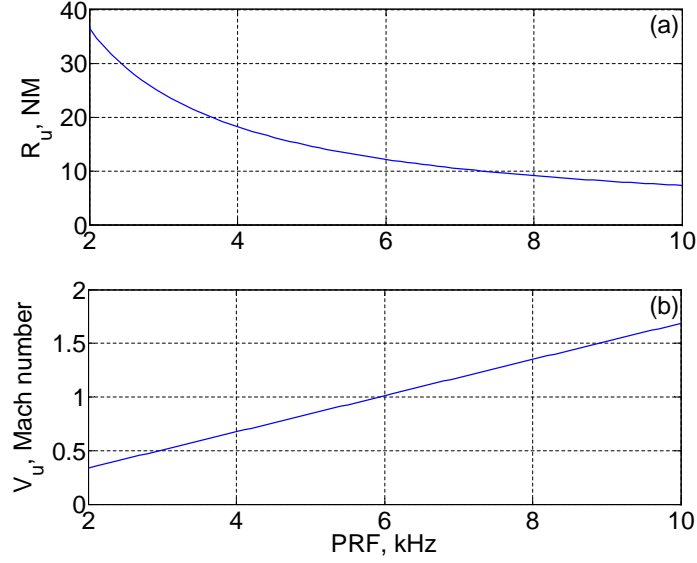


Figure 12: Pulse repetition frequencies versus maximum unambiguous range and maximum unambiguous velocity.

8 Results.

In this section, three options for PRF and waveform design are presented. For each case, the search operation is described, details of waveforms and PRFs are given, and CFAR detection threshold multiplier as well as the overall detection probabilities are computed for a specified false alarm probability, namely, one false alarm every $n_f = 30$ s.

The three cases under consideration are summarised in Table 4. Two different dwell times, i.e., 0.076 s and 0.152 s, are considered. For each dwell time, the 3-of-8 rule is applied. Case 1 and case 3 use one set of PRFs, while case 2 uses two separate sets of PRFs. The CPI of case 3 is double those of case 1 and case 2, while the dwell times of case 2 and case 3 are double that of case 1.

Table 4: The three cases under consideration.

	Beam dwell	CPI	PRF selection
Case 1	0.076 s	0.0095 s	1 set of 8 PRFs
Case 2	2×0.076 s	0.0095 s	2 sets, each of 8 PRFs
Case 3	0.152 s	0.019 s	1 set of 8 PRFs

8.1 Case 1.

8.1.1 Search Operation.

At each beam position, the dwell time is $t_b = 0.076$ s. The frame time is then $9 \times t_b = 0.684$ s. Eight bursts of pulses are transmitted using 8 different PRFs. The pulses in each burst are coherent on transmit and receive. The length of each burst is $t_f = 0.076/8 = 9.5 \times 10^{-3}$ s. If 3 hits are reported on 3 of those 8 PRFs, a target is declared.

8.1.2 PRF and Waveform Selection.

The waveform characteristics are summarised in Table 5, while details of the selected PRFs are shown in Table 6. The PRFs are between 1894 Hz and 7263 Hz, with carrier frequencies from 1270 MHz to 1375 MHz (in 15 MHz steps). The uncompressed pulse-widths are from 13.77 μ s to 52.80 μ s. The pulse compression ratios are from 52 to 198. There are approximately 32000 cells in each RD map.

The range blind zone plots are presented in Fig.13. There are at least 5 clear PRFs between 2 NM to 3.5 NM, and at least 7 clear PRFs between 3.6 NM to 30 NM. The velocity blind zone plots are presented in Fig.14. There are at least 7 clear PRFs up to velocity 650 m/s. The combined range-velocity blind zone plot is shown in Fig.15. There are at least 6 clear PRFs up to velocity ± 400 m/s and out to range 30 NM.

Table 5: Case-1 waveform characteristics.

Duty cycle	0.10
Number of PRFs	8
Carrier gap, MHz	15
Beam dwell, s	0.076
CPI, s	0.0095
Range resolution, m	40
Velocity resolution, m/s	12.1
LFM bandwidth, MHz	3.75
Velocity blind-zone width, m/s	27.2

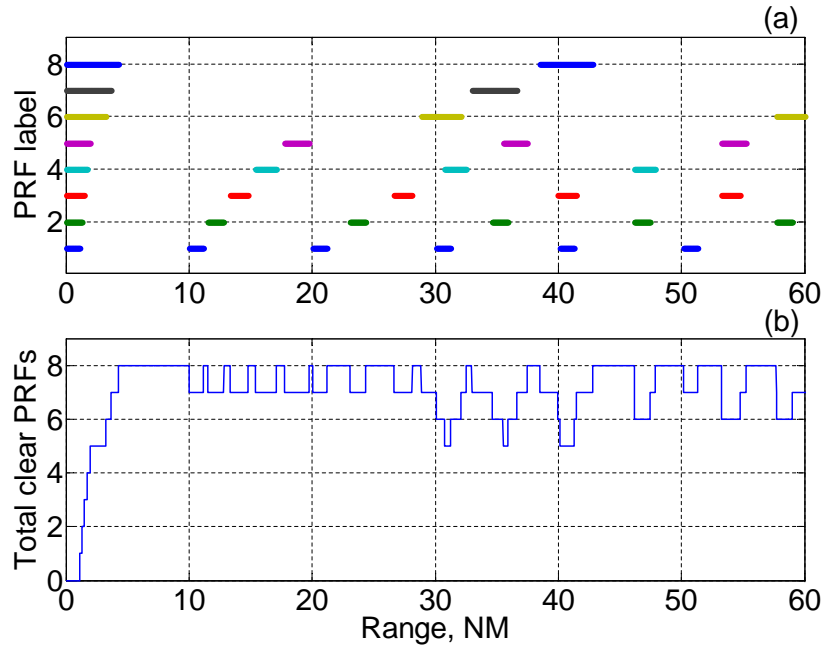
8.2 Case 2.

8.2.1 Search Operation.

At each beam position, the dwell time is $t_b = 0.152$ s. The frame time is then $9 \times t_b = 1.368$ s. Two sets of pulses are transmitted, each set occupies 0.076 s. For each set, 8 bursts of pulses are transmitted using 8 different PRFs, in which the length of each burst is $t_f = 0.076/8 = 0.0095$ s. The pulses in each burst are coherent on transmit and receive. Set 1 is designed for detecting targets from 2 NM to 7 NM, while set 2 is for targets from 7 NM to 20 NM. For each of those two sets, once 3 hits are reported from 3 PRFs, a target is declared.

Table 6: Case-1 PRF parameters.

PRF label	1	2	3	4	5	6	7	8
PRF, Hz	7263	6316	5473	4737	4105	2526	2211	1894
f_c , MHz	1270	1285	1300	1315	1330	1345	1360	1375
Pulse-width, μs	13.77	15.83	18.27	21.11	24.36	39.59	45.23	52.80
R_u , NM	10.04	11.54	13.32	15.39	17.76	28.86	32.97	38.49
Δ_r , NM	1.12	1.28	1.48	1.71	1.97	3.21	3.66	4.28
V_u , m/s	838.0	728.8	631.5	546.6	473.7	291.5	255.1	218.5
Doppler cells	69	60	52	45	39	24	21	18
Range cells	465	534	617	712	822	1336	1526	1782
RD cells	32085	32040	32084	32040	32058	32064	32046	32076
Compression ratio	52	59	69	79	91	148	170	198

**Figure 13:** Range blind-zone plot of case 1.

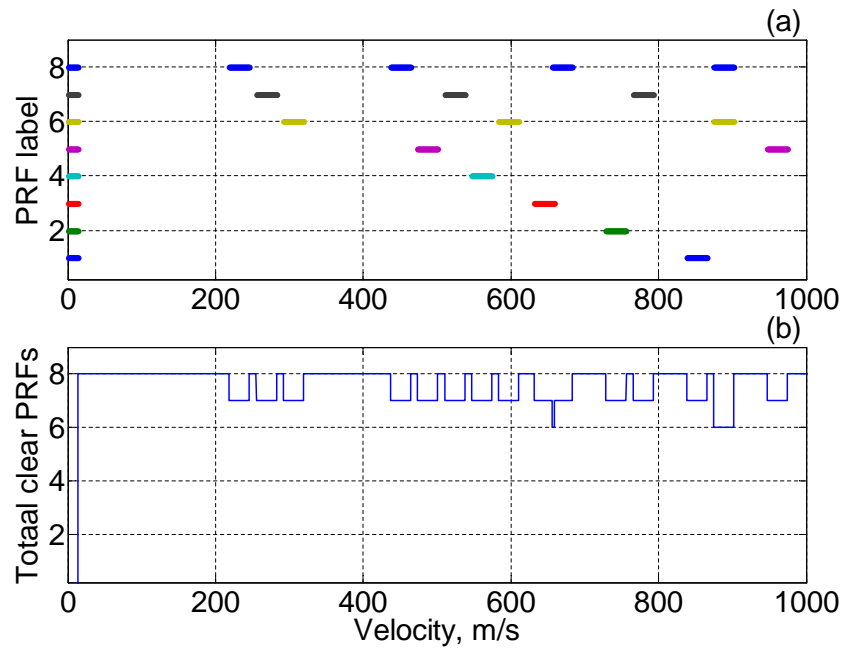


Figure 14: Velocity blind-zone plot of case 1.

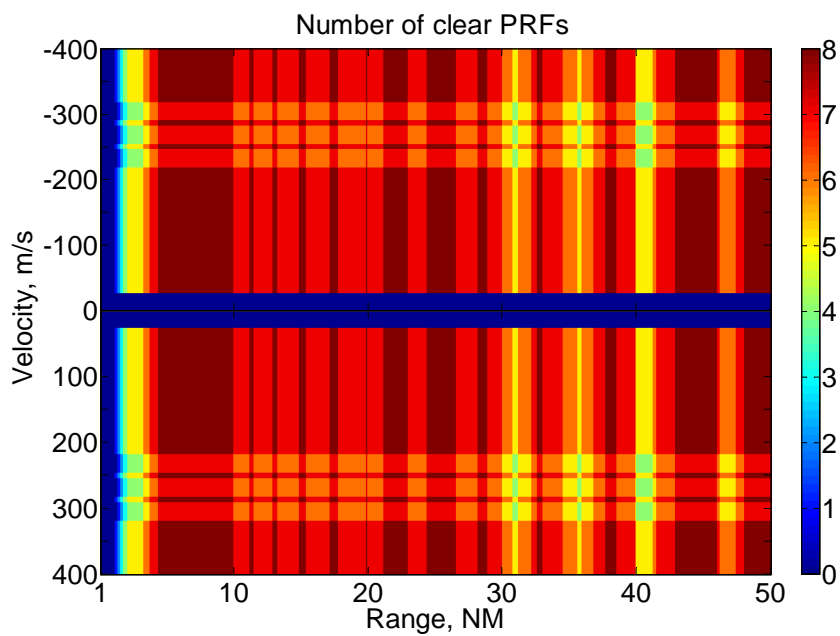


Figure 15: Range-velocity blind-zone plot of case 1.

8.2.2 PRF and Waveform Selection.

For set 1, the waveform characteristics are summarised in Table 7, while details of the PRFs are shown in Table 8. The PRFs are between 10421 Hz and 4316 Hz, with carrier frequencies from 1270 MHz to 1375 MHz (of 15 MHz increment). The uncompressed pulse-widths are from $9.6 \mu\text{s}$ to $23.17 \mu\text{s}$. The pulse compression ratios are from 36 to 87. There are approximately 32000 cells in each range-Doppler map. For set 2, the waveform characteristics are the same as those of set 1 as shown in Table 7, while details of the PRFs are shown in Table 9. The PRFs are between 3684 Hz and 1264 Hz, with carrier frequencies from 1270 MHz to 1375 MHz (of 15 MHz increment). The uncompressed pulse-widths are from $27.14 \mu\text{s}$ to $79.11 \mu\text{s}$. The pulse compression ratios are from 102 to 297. There are approximately 32000 cells in each range-Doppler map.

The range and velocity blind zone plots for set 1 are presented in Fig.16 and Fig.17, respectively. There are 8 clear PRFs from range between 2 NM and 7 NM, whereas there are 8 clear PRFs from velocity between 13 m/s to 500 m/s. The combined range-velocity blind zone plot is shown in Fig.18. There are 7 clear PRFs up to velocity ± 400 m/s and range between 2 to 15 NM.

The range and velocity blind zone plots for set 2 are presented in Fig.19 and Fig.20, respectively. There are 8 clear PRFs from range between 7 NM and 20 NM, and at least 6 clear PRFs from velocity between 13 m/s to 450 m/s. The combined range-velocity blind zone plot is shown in Fig.21. There are at least 6 clear PRFs up to velocity ± 400 m/s and out to range between 7 to 20 NM.

Table 7: Case-2 waveform characteristics.

Duty cycle	0.10
Number of PRFs	8
Carrier gap, MHz	15
Beam dwell (set-1 + set-2), s	$0.076 + 0.076$
CPI, s	0.0095
Range resolution, m	40
Velocity resolution, m/s	12.1
LFM bandwidth, MHz	3.75
Velocity blind-zone width, m/s	27.2

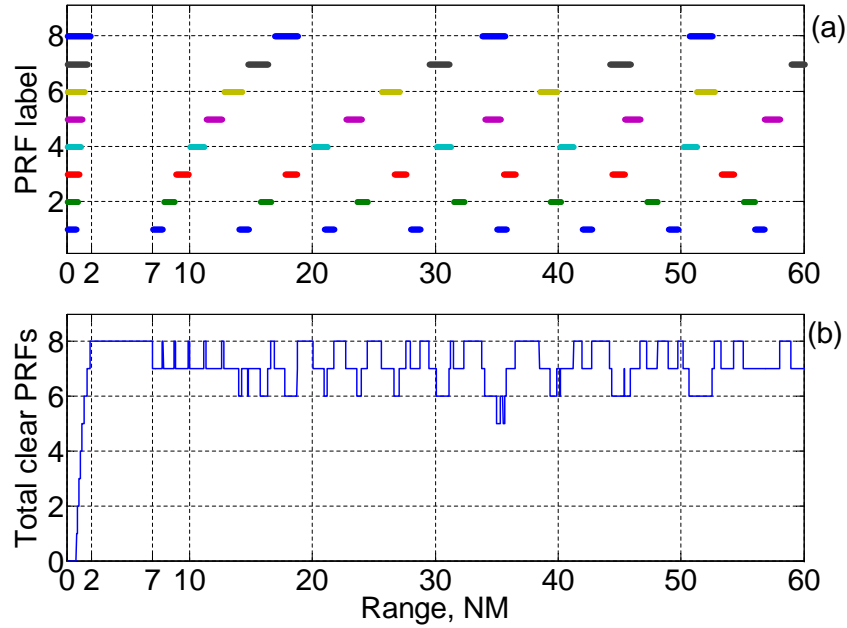
8.3 Case 3.

8.3.1 Search Operation.

At each beam position, the dwell time is $t_b = 0.152$ s. The frame time is then $9 \times t_b = 1.368$ s. Eight bursts of pulses are transmitted using 8 different PRFs. The pulses in each burst are coherent on transmit and receive. The length of each CPI is $t_f = 0.152/8 = 19 \times 10^{-3}$ s. Once 3 hits are reported on 3 of those 8 PRFs, a target is declared.

Table 8: PRF parameters of case 2, PRF set 1.

PRF label	1	2	3	4	5	6	7	8
PRF, Hz	10421	9264	8211	7264	6422	5685	4947	4316
f_c , MHz	1270	1285	1300	1315	1330	1345	1360	1375
Pulse-width, μs	9.60	10.79	12.18	13.77	15.57	17.59	20.21	23.17
R_u , NM	6.99	7.87	8.88	10.03	11.35	12.82	14.74	16.89
Δ_r , NM	0.78	0.87	0.99	1.11	1.26	1.42	1.64	1.88
V_u , m/s	1202.4	1068.9	947.4	838.2	741.0	656.0	570.8	498.0
Doppler cells	99	88	78	69	61	54	47	41
Range cells	324	364	411	465	526	594	682	782
RD cells	32076	32032	32058	32085	32086	32076	32054	32062
Compression ratio	36	40	46	52	58	66	76	87

**Figure 16:** Range blind-zone plot of case 2, PRF set 1.

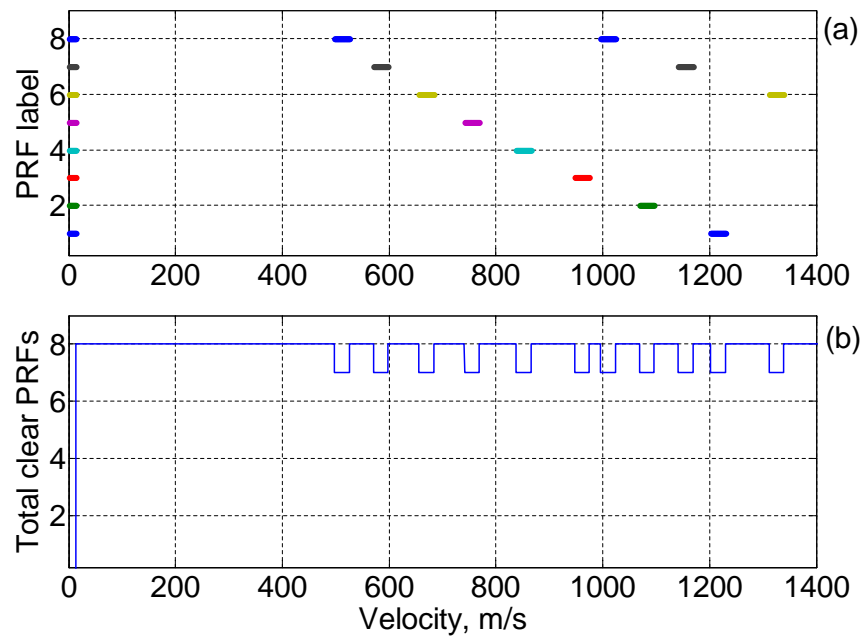


Figure 17: Velocity blind-zone plot of case 2, PRF set 1.

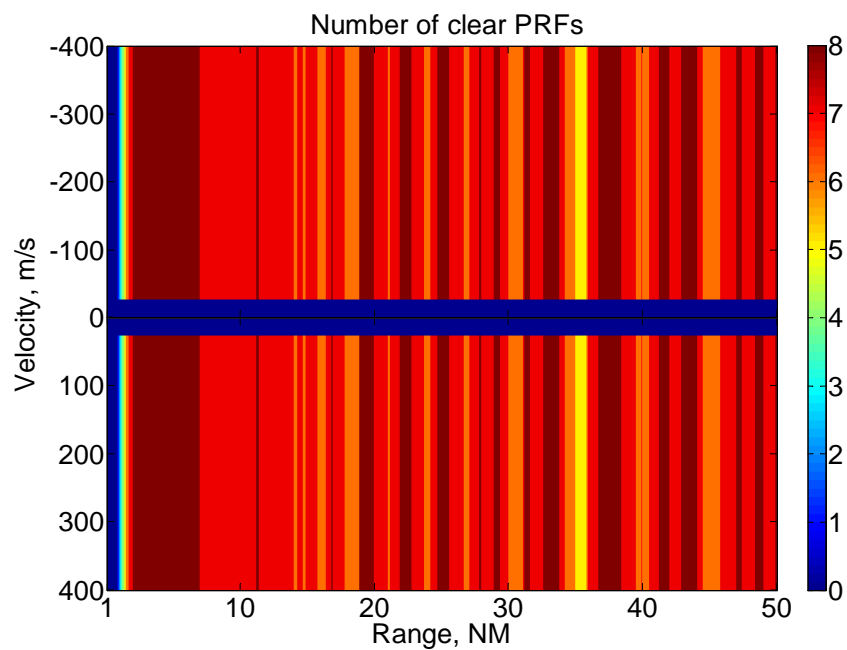
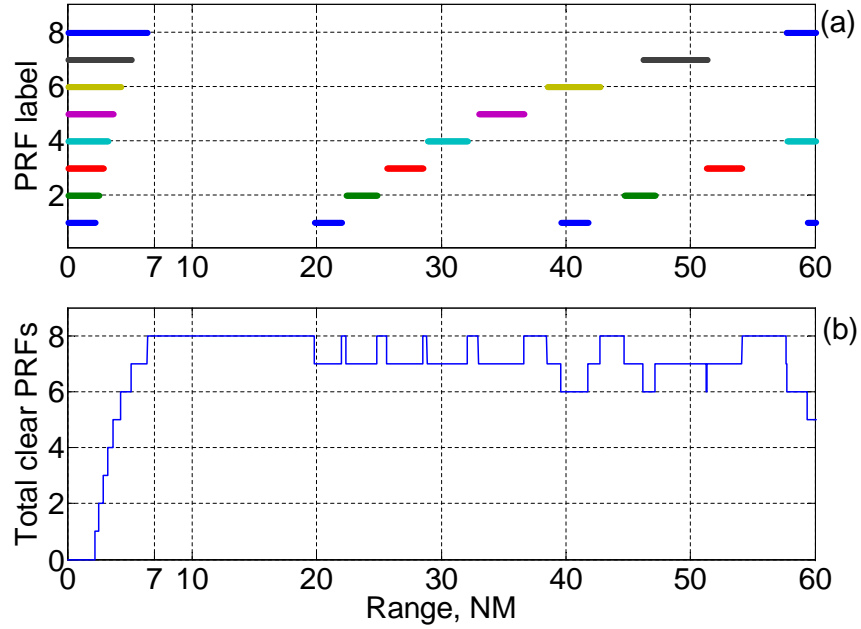


Figure 18: Range-velocity blind-zone plot of case 2, PRF set 1.

Table 9: PRF parameters of case 2, PRF set 2.

PRF label	1	2	3	4	5	6	7	8
PRF, Hz	3684	3264	2843	2526	2211	1895	1578	1264
f_c , MHz	1270	1285	1300	1315	1330	1345	1360	1375
Pulse-width, μs	27.144	30.637	35.174	39.588	45.228	52.770	63.371	79.114
R_u , NM	19.79	22.33	25.64	28.86	32.97	38.47	46.19	57.67
Δ_r , NM	2.20	2.48	2.85	3.21	3.66	4.27	5.13	6.41
V_u , m/s	425.1	376.6	328.0	291.5	255.1	218.7	182.1	145.8
Doppler cells	35	31	27	24	21	18	15	12
Range cells	916	1034	1187	1336	1526	1781	2139	2670
RD cells	32060	32054	32049	32064	32046	32058	32085	32040
Compression ratio	102	115	132	148	170	198	238	297

**Figure 19:** Range blind-zone plot of case 2, PRF set 2.

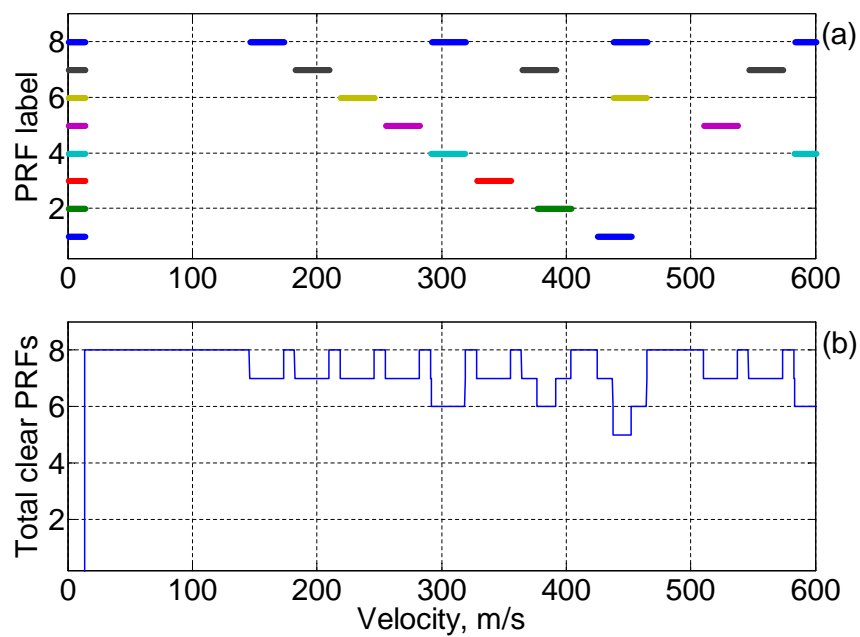


Figure 20: Velocity blind-zone plot of case 2, PRF set 2.

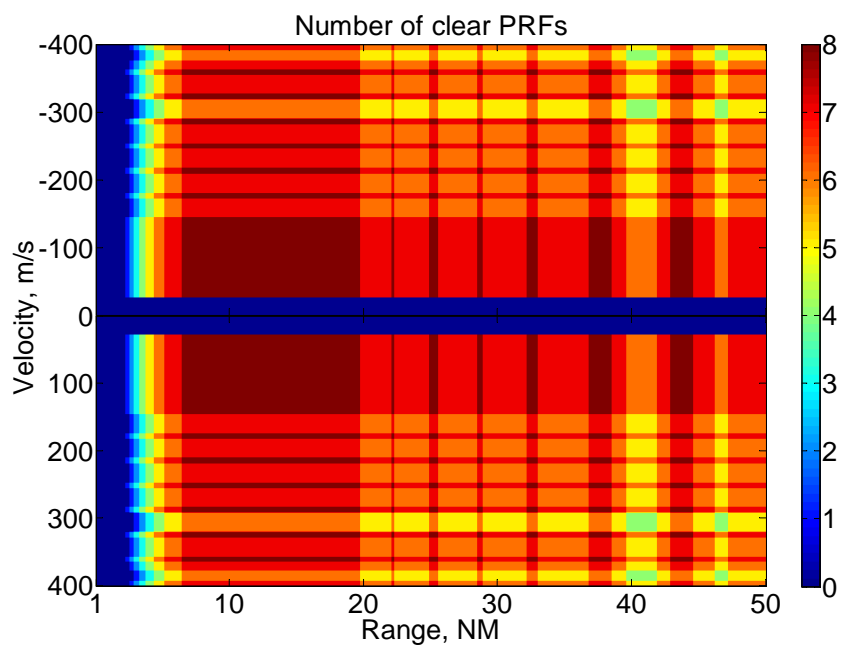


Figure 21: Range-velocity blind-zone plot of case 2, PRF set 2.

8.3.2 PRF and Waveform Selection.

The waveform parameters are summarised in Table 10, while details of the selected PRFs are shown in Table 11. The PRFs are between 7263 Hz and 1948 Hz, with carrier frequencies from 1270 MHz to 1375 MHz (of 15 MHz steps). The uncompressed pulse-widths are from $13.77 \mu\text{s}$ to $51.34 \mu\text{s}$. The pulse compression ratios are from 52 to 198. There are approximately 64100 cells in each range-Doppler map.

The range blind zone plots are presented in Fig.22. There are at least 5 clear PRFs between 2 NM to 3.5 NM, and at least 7 clear PRFs between 3.6 NM to 30 NM. The velocity blind zone plots are presented in Fig.23. There are at least 7 clear PRFs up to velocity 650 m/s. The combined range-velocity blind zone plot is shown in Fig.24. There are at least 4 clear PRFs at range between 2 to 4 NM, and at least 6 clear PRFs at range between 4 to 30 NM.

Table 10: Case-3 waveform characteristics.

Duty cycle	0.10
Number of PRFs	8
Carrier gap, MHz	15
Beam dwell, s	0.152
CPI, s	0.019
Range resolution, m	40
Velocity resolution, m/s	6.0
LFM bandwidth, MHz	3.75
Velocity blind-zone width, m/s	27.2

Table 11: Case-3 PRF parameters.

PRF label	1	2	3	4	5	6	7	8
PRF, Hz	7263	6263	5527	4737	4158	2526	2211	1948
f_c , MHz	1270	1285	1300	1315	1330	1345	1360	1375
Pulse-width, μs	13.768	15.967	18.093	21.110	24.050	39.588	45.228	51.335
R_u , NM	10.04	11.64	13.19	15.39	17.53	28.86	32.97	37.42
Δ_r , NM	1.12	1.29	1.47	1.71	1.95	3.21	3.66	4.16
V_u , m/s	838.0	722.7	637.7	546.6	479.8	291.5	255.1	224.8
Doppler cells	138	119	105	90	79	48	42	37
Range cells	465	539	611	712	812	1336	1526	1733
RD cells	64170	64141	64155	64080	64148	64128	64092	64121
Compression ratio	52	60	68	79	90	148	170	193

8.4 Target Detection Probability.

The false alarms and target detection probabilities are computed as follows.

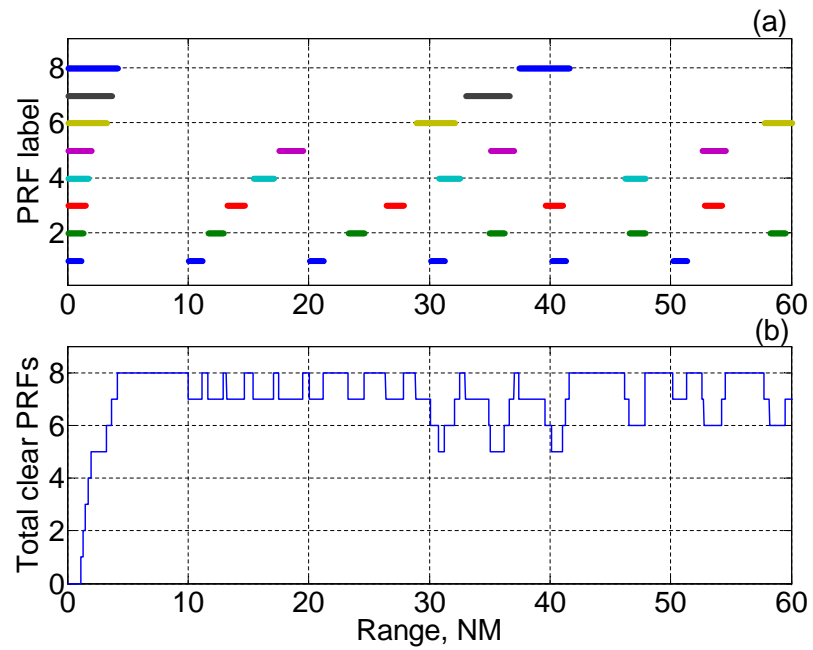


Figure 22: Range blind-zone plot of case 3.

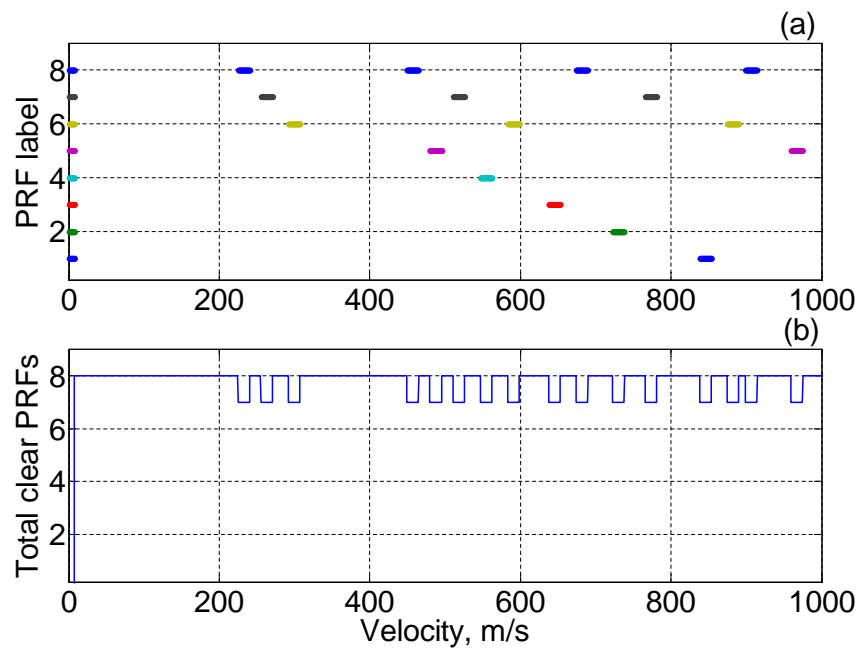


Figure 23: Velocity blind-zone plot of case 3.

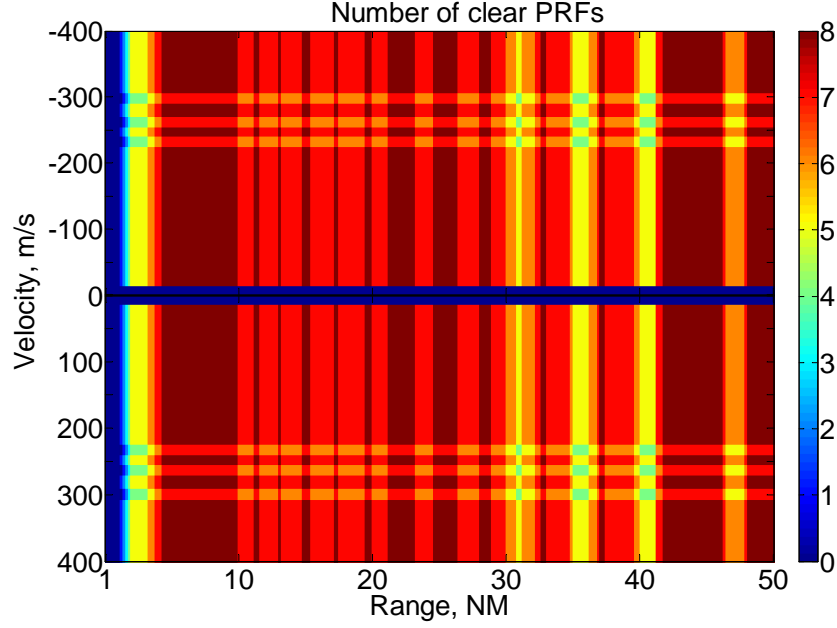


Figure 24: Range-velocity blind-zone plot of case 3.

- False alarm rates:

- (i) To give one false alarm every n_f seconds, the false alarm rate F_a at each beam location is the inverse of the total number of cell detections performed in n_f seconds, i.e.,

$$F_a = \frac{1}{\left(\frac{n_f}{t_b}\right) n} \quad (31)$$

where t_b is the dwell time of each beam; and n is the number of range-velocity resolution cells to be checked at each beam, which can be computed as:

$$n = [(R_{max} - R_{min})/\Delta R] \times [2(V_{max} - V_{min})/\Delta V] \quad (32)$$

where R_{max} and R_{min} are the maximum and minimum ranges, respectively; V_{max} and V_{min} are the maximum and minimum velocities, respectively; and ΔR and ΔV are the range and velocity resolutions, respectively. For the computation of target detection probability in this section, $R_{max} = 30$ NM, $R_{min} = 2$ NM, $V_{max} = 340$ m/s (Mach-1), $V_{min} = 13.5$ m/s.

- (ii) The CA-CFAR false alarm F_{CA} is computed by iteratively solving equation (17) in which $P_{fa} = F_a$, $M = 3$, and $N = 8$.
- (iii) The CA-CFAR threshold multiplier T is computed substituting F_{CA} into equation (14) in which $L_{CA} = 24$.
- Target detection probability:

- (iv) At each range R , target SNR is computed using equation (13).
- (v) CA-CFAR detection probability P_{CA} is computed by substituting T in step (iii) and target SNR in step (iv) into equation (15).
- (vi) The overall target detection probability P_D is computed by substituting P_{CA} calculated in step (v) into equation (18).

The overall false alarm F_a , the CA-CFAR false alarm F_{CA} , and the CA-CFAR detection threshold multipliers for three cases are summarised in Table 12. Refer to equations (31) and (32):

- Case 1 and case 3 have the same overall false alarm F_a , since although the dwell time t_b of case 3 is twice that of case 1, the velocity resolution of case 3 is also 2 times finer than that of case 1 (see Table 11 and Table 6).
- The overall false alarm F_a of case 2 is twice that of case 1. This is because the dwell time t_b of case 2 is twice that of case 1, while the velocity resolution of case 2 is the same as that of case 1 (see Table 9 and Table 6).

Table 12: *Detector parameters.*

	False alarm F_a	CA-CFAR false alarm	CA-CFAR multiplier T
Case 1	3.59×10^{-8}	8.64×10^{-4}	0.3417
Case 2	7.18×10^{-8}	1.09×10^{-3}	0.3287
Case 3	3.59×10^{-8}	8.64×10^{-4}	0.3417

Target detection probabilities for the three cases with maximum 8 clear PRFs are shown in Fig.25. For all three cases, target detection probabilities above 90% are achieved at ranges up to 7 NM (i.e., around Parafield airport), 12.5 NM (between Adelaide CBD and Adelaide airport), and 22.5 NM (approximately 5 NM away from Adelaide airport) for targets of RCS 1 m², 10 m², and 100 m², respectively. It is observed that case 1 and case 2 have the same detection performance, while case 3 has a superior performance. The reason is that in case 3, the CPI is twice longer than those of case 1 and case 2, giving a 3 dB improvement in target SNR as evident in Fig.26.

Target detection probabilities for cases 1 and 2 with different number of clear PRFs are shown in Fig.27. At least 6 clear PRFs are required in order to achieve a target detection probability above 90% for targets of RCS 1, 10, and 100 m² at ranges around 7 NM, 12 NM, and 20 NM, respectively. Target detection probabilities for case 3 with different number of clear PRFs are shown in Fig.28. It is observed that the same detection performance as those of cases 1 and 2 can be achieved with at least 5 clear PRFs.

In summary, for all three cases, the dwell time is long enough for achieving target detection probabilities above 90% at ranges of interest for targets of interest. For cases 1 and 3, targets at far ranges have to compete with clutter at closer ranges. This restriction is relaxed in case 2 with the use of two sets of PRFs. In addition, for case 3: (i) target detection is 3 dB better than those of cases 1 and 2; and (ii) velocity resolution is also half of those of cases 1 and 2. However, the frame-time of cases 2 and 3 is twice that of case 1.

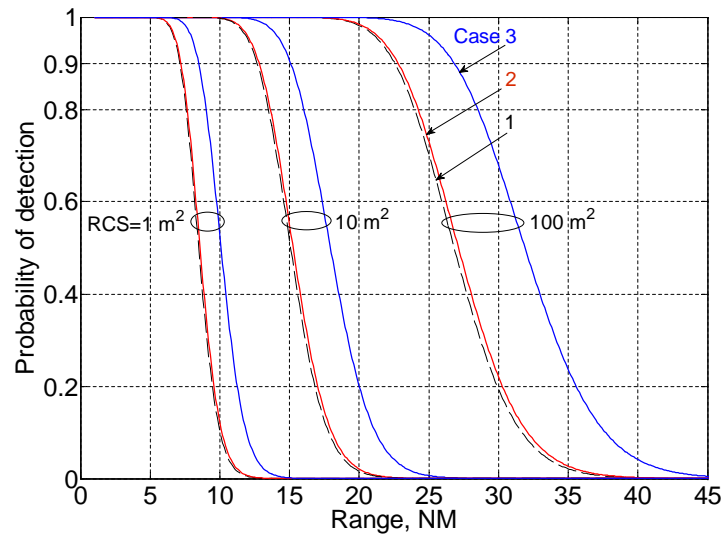


Figure 25: Target detection probability of three cases with 8 clear PRFs.

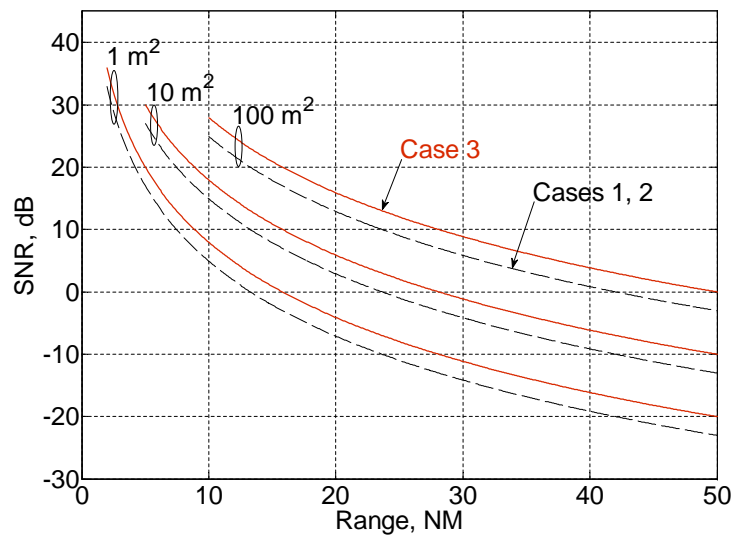


Figure 26: Target SNR for RCS of 1, 10, and 100 m².

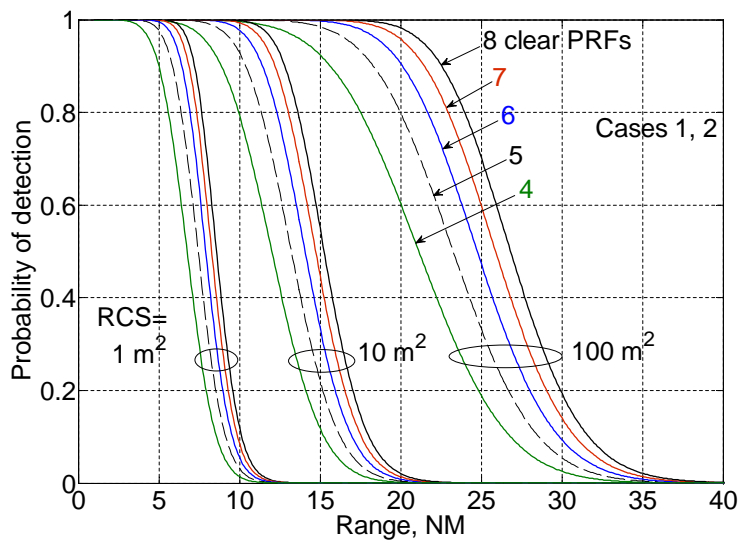


Figure 27: Cases 1 & 2 target detection probability with different number of clear PRFs.

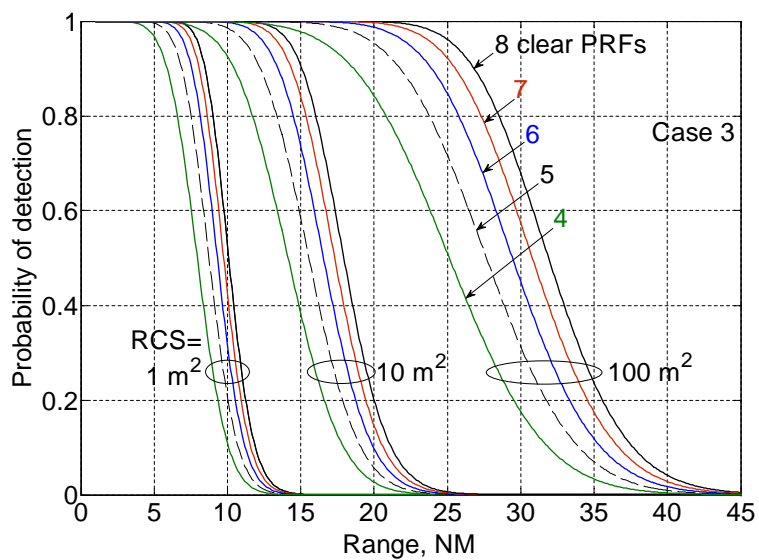


Figure 28: Case-3 target detection probability with different number of clear PRFs.

9 Dynamic Range.

The efficiency of a detection algorithm depends on the clutter input level and clutter attenuation. In this section, the limitation on clutter attenuation due to oscillator phase noise is addressed. Clutter input level due to distributed land clutter, distributed hill clutter, and discrete land clutter are also characterised.

9.1 Effect of Oscillator Phase Noise.

For pulsed-Doppler radar systems, the clutter attenuation limit is set by the stability of the stable local oscillator (STALO) [5]. The clutter residue is determined by the phase noise in the oscillators from which both transmitted and received signals are derived.

Clutter attenuation is defined as the ratio between the output clutter C_o and the input clutter C_i . In the presence of phase noise, the ratio C_o/C_i is given by [6], p251:

$$\frac{C_o}{C_i} = B_f \left(\frac{B}{PRF} \right) (2W_0) \quad (33)$$

where B_f is the Doppler filter bandwidth defined as $B_f = 1/t_f$, where t_f is the coherent processing time; B is the bandwidth of the matched filter (eg., compression filter); PRF is the pulse repetition frequency; W_0 is the phase noise spectrum density; the multiplication factor of 2 is the correlation factor (details of correlation factors for common oscillator in pulsed-Doppler radar can be found in [6], pp249-250).

For instance, consider the case with a CPI of $t_f = 0.076$ s which gives a Doppler filter bandwidth of $B_f = 1/t_f = 1/0.076 = 13.2$ Hz; for a compression filter of bandwidth $B = 4$ MHz and a $PRF = 2000$ Hz, there are $B/PRF = 4 \times 10^6 / 2 \times 10^3 = 2000$ sidebands aliased to the filter. For the XPAR2 system, the phased noise sidebands are experimentally plotted as spectral density (on dB scale) below the carrier frequency per hertz and shown in Fig.B1 of Appendix B. Most of the clutter power comes from the flat spectrum (between 1.5 kHz and 30 kHz) with density $W_0 \approx -90$ dBc/Hz. From equation (33):

$$\frac{C_o}{C_i} = B_f \left(\frac{B}{PRF} \right) (2W_0) = 13.2 \times 2000 \times 2 \times 10^{-9.0} = -42.8 \text{ dB} \quad (34)$$

The limiting level for clutter attenuation is then 42.8 dB, assume that there are no other contributions to the clutter residue.

From a waveform and PRF selection point-of-view, equation (33) suggests that clutter attenuation C_o/C_i can be made smaller by (i) designing RD-map cells with finer Doppler resolution B_f by employing longer CPI, (ii) designing RD-map cells with courser range resolution so that the compression filter bandwidth B is smaller, and (iii) employing high PRFs where possible so that there is a smaller number of side-bands aliased into the Doppler filter.

Clutter attenuation with PRFs from 1 kHz to 10 kHz for the above three design cases are shown in Fig.29 for phase noise density $W_0 = -90$ dBc/Hz. It is observed that for the same PRF, different selections of waveforms can give a 3 dB difference in

clutter attenuation level as evident in the discrepancy between the cases 1 and 2 curve ($t_f = 0.0095$ s, $B_f = 105$ Hz, $B = 3.75$ MHz) and the case 3 curve ($t_f = 0.019$ s, $B_f = 52.6$ Hz, $B = 3.75$ MHz). In addition, the use of a high PRF (eg., 10 kHz) can save up to 7 dB in clutter attenuation compared with the use of a low PRF (eg., 2 kHz).

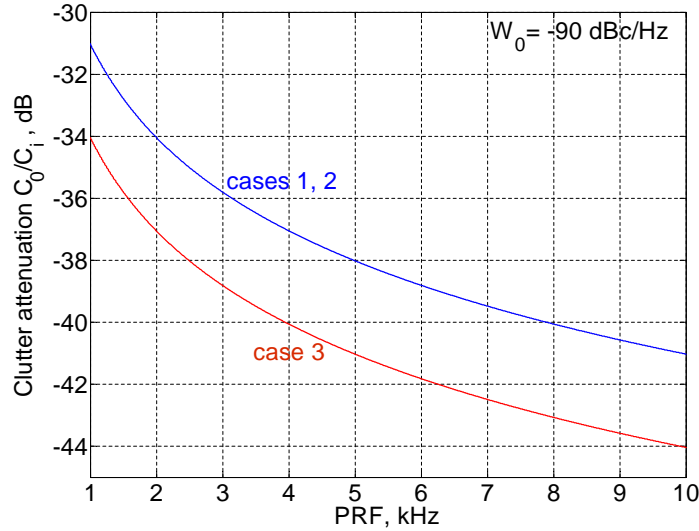


Figure 29: Limitation of clutter attenuation due to phase noise.

9.2 Effect of Clutter.

From an originating source point-of-view, clutter can be classified into three types [6]: (i) distributed clutter in which clutter sources are distributed over a surface (eg., land or sea), (ii) volume clutter in which clutter sources are dispersed within a volume (eg., weather or chaff), or (iii) discrete clutter in which clutter sources concentrate at various discrete points (eg., building towers, power lines, water tanks). In this report, the constant- γ model is employed for characterising distributed ground clutter. For discrete ground clutter, discrete clutter points are treated as isolated targets which are characterised by RCS [6], pp108-123.

9.2.1 Overview of Constant- γ Clutter Model.

For distributed ground clutter, a model that offers excellent agreement with most experimental data measured at grazing angles away from 90 degrees is the constant- γ model which is characterised by the reflectivity σ^0 described as [6]:

$$\sigma^0 = \gamma \sin \psi \quad (35)$$

where ψ is the grazing angle; and γ is a parameter which accounts for the scattering property of the surface and is almost independent from the radar wavelength.

Variations in land clutter reflectivity with wavelength is modeled by the propagation factor F_c which is computed as follows. Define the critical grazing angle as:

$$\psi_c = \frac{\lambda}{4\pi\sigma_h} \quad (36)$$

where λ is the wavelength and σ_h is the root-mean-square (rms) surface height deviation from the average height.

- For grazing angle $\psi \geq \psi_c$:

$$F_c = 1 \quad (37)$$

- For grazing angle $\psi < \psi_c$:

$$F_c = \frac{\psi}{\psi_c} \approx \frac{R_1}{R} \quad (38)$$

where R is range and R_1 is the range at the critical grazing angle. R_1 is related to the radar height h_r above the surface according to:

$$R_1 = \frac{4\pi\sigma_h h_r}{\lambda} \quad (39)$$

The surface reflectivity near vertical incident (i.e., at $\psi \approx 90$ degrees) is:

$$\sigma_f = \left(\frac{\rho}{\beta_0}\right)^2 \exp\left[-\left(\frac{\pi/2 - \psi}{\beta_0}\right)^2\right] \quad (40)$$

where $\rho = 0.5$ is the Fresnel coefficient at vertical incidence, and β_0 is the rms slope of the surface.

The total land reflectivity is then:

$$\sigma_{total}^0 = \sigma^0 F_c^4 + \sigma_f \quad (41)$$

The land surface parameters γ , σ_h , and β_0 for different surface types (such as mountain, farmland, etc.) are summarised in Table C1 in Appendix C.

Land reflectivity for XPAR-2 radar at frequency 1.3 GHz is computed using (41) and shown in Fig.30. Reflectivity of mountain and urban clutter is approximately 10 dB above that of the farmland.

9.2.2 Discrete Ground Clutter.

For discrete ground clutter, several models have been proposed. A model that was proposed for general use is summarised in Table 13, in which the density (per km²) of discrete clutter sources is shown for different clutter RCS values [6], p122.

The discrete clutter-to-noise ratio (CNR) is computed using the radar equation:

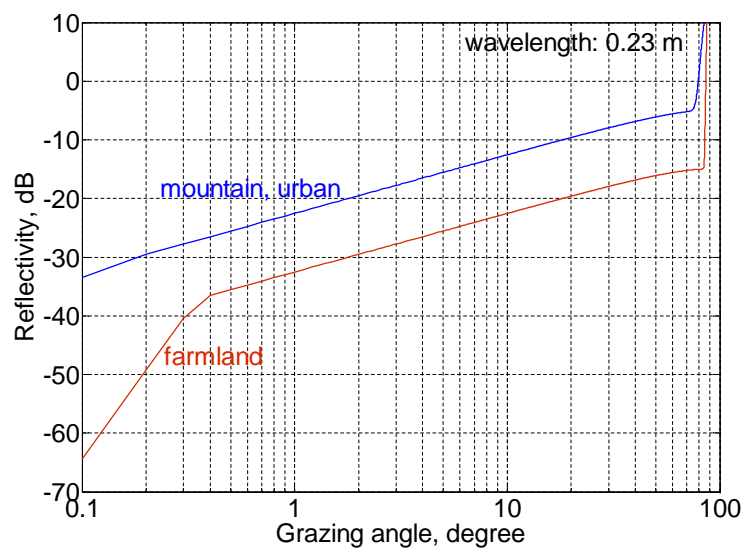


Figure 30: Land clutter reflectivity σ_{total}^0 at frequency 1.3 GHz.

Table 13: Model for discrete ground clutter [22].

Density per km ² area	Cross section, m ²
2	10 ²
0.5	10 ³
0.2	10 ⁴

$$CNR = \frac{P_{av} t_f G_t G_r \lambda^2 \sigma_c}{(4\pi)^3 k T L R^4} \quad (42)$$

Equation (42) is the same as the radar equation (13) where $\sigma = \sigma_c$ which is the total RCS of the discrete sources within a (compressed) range resolution cell. Using Table 13, σ_c is computed as follows:

$$\begin{aligned} \sigma_c &= (2 \times 10^2 + 0.5 \times 10^3 + 0.2 \times 10^4) A(R) \\ A(R) &= \Delta R R \Theta_a / 10^6 \end{aligned} \quad (43)$$

where $A(R)$ is the area of the illuminated clutter patch normalised to km^2 (i.e., 10^6 m^2); ΔR is the compressed range resolution; R is the range of the clutter patch; and Θ_a is the azimuth 3 dB beamwidth.

The power received by the radar from the discrete clutter points within a range resolution cell at range R is computed as [5], p11:

$$S_t = \frac{P_t G_t G_r \lambda^2 \sigma_u}{(4\pi)^3 R^4} \quad (44)$$

where σ_u is computed similarly to σ_c of equation (43) in which ΔR is the range resolution before pulse compression; P_t is the transmission peak power, while other parameters are as described in (13).

For $\Theta_a = 20.2$ degrees (beam 1 of Table 1) and an uncompressed pulse width of $50 \mu\text{s}$ (the longest pulse in Case 3 of Table 11, which corresponds to an uncompressed range cell of 7500 m), the estimated CNR and the radar received power due to discrete clutter are shown in Fig.31(a) and (b), respectively. Since the worst clutter attenuation is around 35 dB (see Fig.29), clutter discretises are suppressed to below the noise floor at ranges longer than 12 NM (marked by the arrow in Fig.31(a)). At range closer than 5 NM, clutter residues can be as high as 20 dB. As shown in Fig.31(b), the radar received power is well below the specified limit of -25 dBm .

Based on this discrete clutter model, it is anticipated that on the radar screen there may exist isolated bright regions of high contrast corresponding to locations of discrete clutter points with large RCSs. If an aircraft happens to flight above those large RCS clutter discretises, then the problem is that it may not be detected. Methods for circumvent this discrete clutter problem include the use of limiter and the use of a dual-beam system (i.e., the electronically steered elevation angles of the transmit and receive beams are slightly different) [5].

9.2.3 Distributed Ground Clutter.

A ground-based radar clutter geometry is described in Fig.32. From this geometry, the clutter area is first calculated, and the clutter RCS is then computed. The main-beam clutter area, A_M , and the side-lobe clutter area, A_S are:

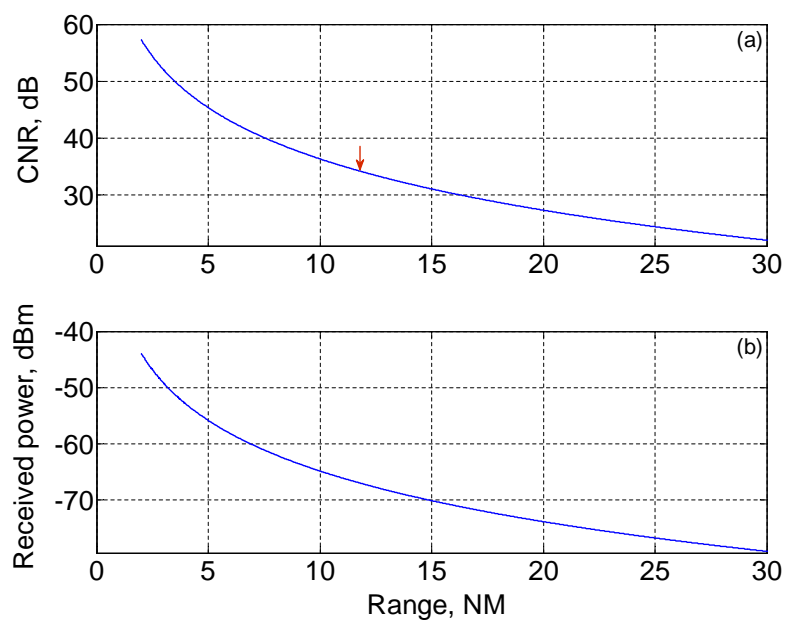


Figure 31: Discrete clutter CNR and the corresponding received power, $CPI = 0.019$ s.

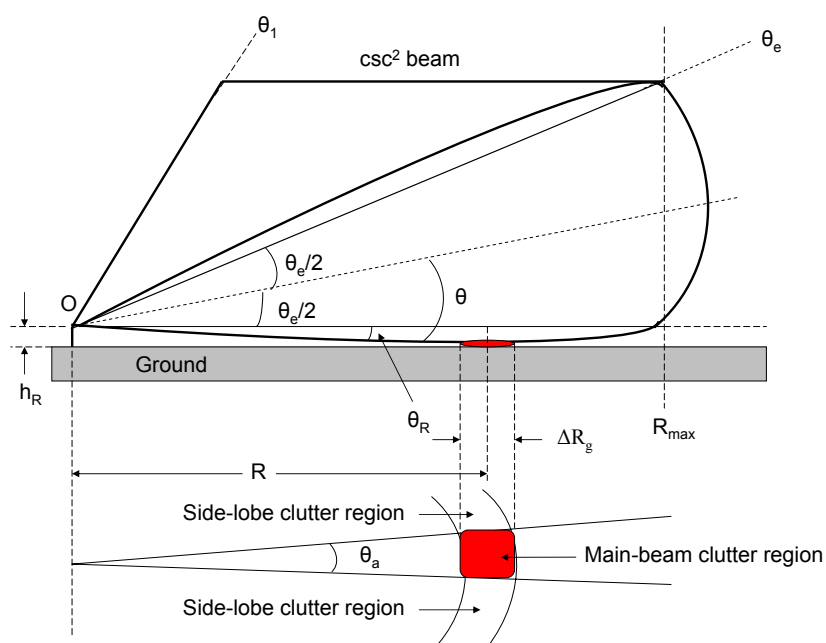


Figure 32: Ground-based radar clutter geometry.

$$\begin{aligned}
A_M &= \Delta R_g R_g \theta_a \\
A_S &= \Delta R_g \pi R_g
\end{aligned} \tag{45}$$

where:

$$\begin{aligned}
R_g &= R \cos \theta_R \\
\theta_R &= \arcsin(h_r/R) \\
\Delta R_g &= \Delta R \cos \theta_R
\end{aligned} \tag{46}$$

If we approximate the centre of the antenna pattern as a Gaussian, the antenna gain at the clutter area (at range R) on the ground is:

$$G(\theta) = \exp\left(\frac{-2.776\theta^2}{\theta_e^2}\right) \tag{47}$$

where the number -2.776 is selected such that the antenna 3 dB beamwidth is θ_e , and θ is a measure of how far the clutter patch at range R deviates from the antenna (elevation) broadside:

$$\theta = \theta_e/2 + \theta_R = \theta_e/2 + \arcsin(h_r/R) \tag{48}$$

The main-lobe clutter RCS σ_M and the side-lobe clutter RCS σ_S are:

$$\begin{aligned}
\sigma_M &= \sigma^0 A_M G^2(\theta) = \sigma^0 \Delta R_g R_g \theta_a G^2(\theta) \\
\sigma_S &= \sigma^0 A_S (S_{rms})^2 = \sigma^0 \Delta R_g \pi R_g (S_{rms})^2
\end{aligned} \tag{49}$$

where S_{rms} is the root-mean-squared (rms) of the side-lobe level. Using the constant- γ model, σ^0 is replaced by σ_{total}^0 given in equation (41). The combined main-lobe, side-lobe clutter RCS is then:

$$\sigma_c = \sigma_M + \sigma_S \tag{50}$$

Substitute $\sigma = \sigma_c$ of equation (50) into equation (13), the CNR is then:

$$CNR = \frac{P_{av} t_f G_t G_r \lambda^2 \sigma_c}{(4\pi)^3 k T L R^4} \tag{51}$$

9.2.4 Distributed Hill Clutter.

As shown in Fig.1, the foothill border aligns in the south-west to north-east direction and is at least 10 NM from the radar. A side-view of the radar beam and the hill clutter geometry is shown in Fig.33. The radar is at point O which is at height h_R above the ground. The radar beam reaches the hill at point A inside the radar 3 dB elevation beamwidth. The hill surface forms an angle α with the ground surface. Point A is at range R from the radar and is on the surface which is parallel to the ground surface and at height h_R above the ground surface. Denote this surface as the $OA h_R$ surface. For each radar resolution cell, the hill clutter area is the sum of the component above the $OA h_R$ surface and the component $AX = h_R \sec(\alpha)$ below the $OA h_R$ surface. In this application, for $h_R = 3.5$ m and $\alpha \approx 30$ degrees, $AX \approx 7$ m, i.e., much smaller than the range resolution cell of 40 m. For this reason, the component below the $OA h_R$ surface is ignored.

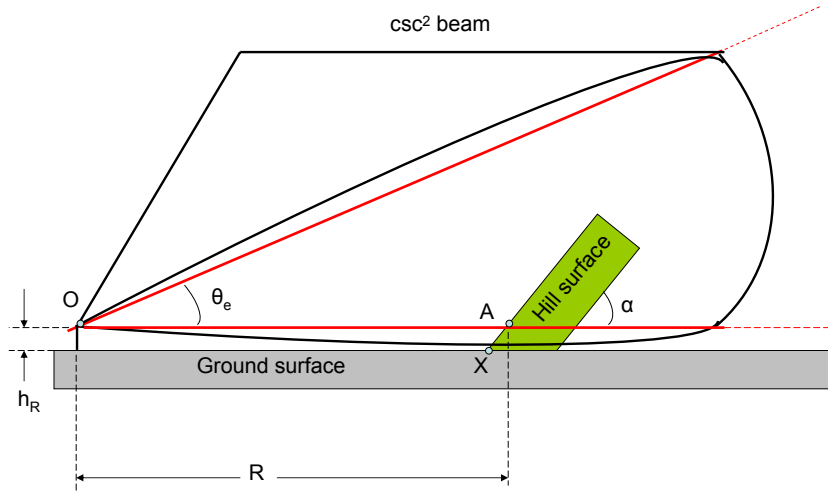


Figure 33: Ground-based radar hill clutter geometry.

In the following analysis, the $OA h_R$ surface is also called the ground surface for simplicity. In addition, since the distance OA (from the radar to the hill) is greater than 10 NM while the radar height h_R is only 3.5 m, $\Delta R \approx \Delta R_g$ in equation (46).

The top-view of the hill clutter geometry is shown in Fig.34. The radar is located at the far end and points its beam towards the hill. The 3 dB azimuth beamwidth is θ_a . One edge of the beam intersects with the hill-ground border and the hill-top line at points A and A_0 , respectively (forming an angle β with the hill-ground border); the other edge of the beam intersects with the hill-ground border and the hill-top line at points Z and Z_0 , respectively (forming an angle $\beta_1 = \beta - \theta_a$ with the hill-ground border). The part of the

hill that is illuminated by the radar beam is the trapezium AA_0Z_0Z which is divided into strips of depth ΔR (i.e., the range resolution).

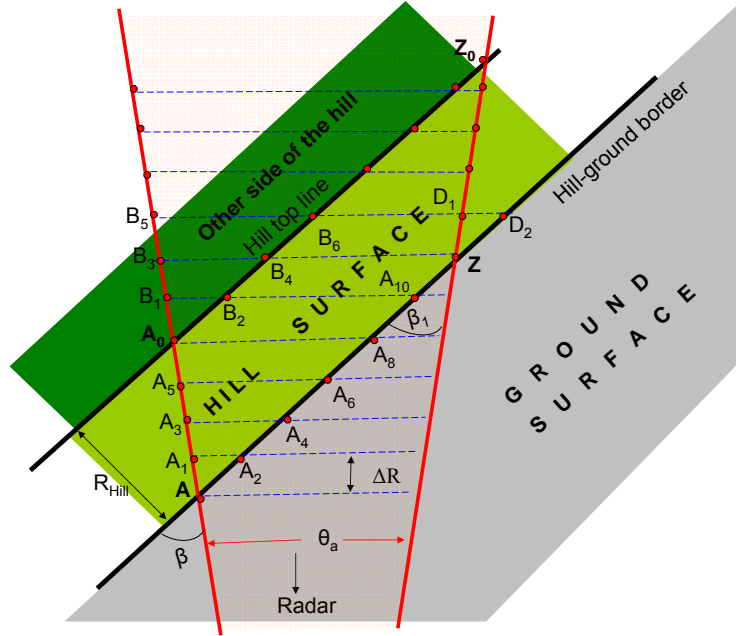


Figure 34: Top-view of hill clutter geometry.

The hill clutter geometry in three-dimension (3D) is illustrated in Fig.35. The hill surface forms an angle α with the ground. The clutter patches are shown in strips of depth ΔR and extend across the antenna 3 dB azimuth beamwidth θ_a . Due to the orientation of the hill, only a small section of each of these range resolution strips overlaps with the hill surface.

Let:

$$\begin{aligned} k_1 &= h_0 / (\tan \alpha \sin \beta \Delta R) \\ k_2 &= (R_1 - R_0) / \Delta R \end{aligned} \quad (52)$$

where h_0 is the height of the hill (i.e., the distance from the hill-top line to the ground); R_0 and R_1 is the range from the radar to points A and Z , respectively. R_1 is computed as:

$$R_1 = R_0 \sin \beta / \sin \beta_1 \quad (53)$$

Parameter k_1 accounts for the limit of the hill clutter area due to the hill-top line, while k_2 is set to keep the hill clutter area within the 3 dB azimuth beamwidth. The area of the hill-clutter patch at range $R = R_0 + k\Delta R$, $k = 1, 2, \dots$, is (see Appendix D for detailed calculation).

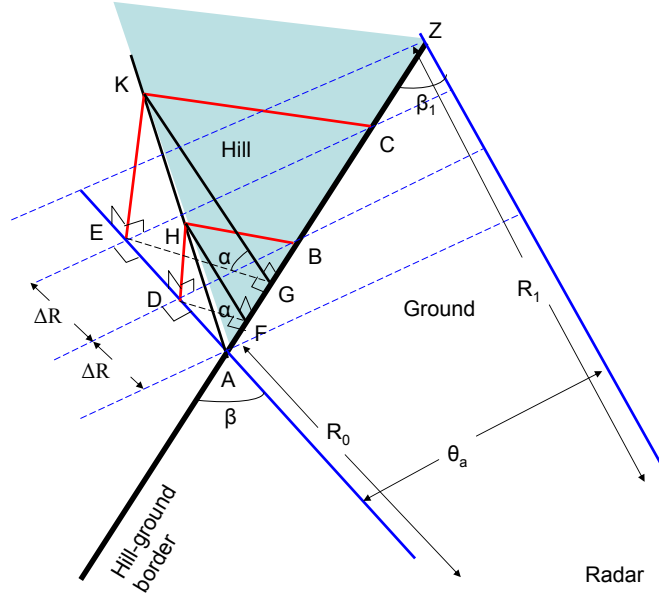


Figure 35: Hill clutter geometry in 3D view.

- If $k \leq k_1$, then

$$A_k = (k - 0.5)(\Delta R)^2 \sec \alpha \tan \beta \quad (54)$$

- If $k_1 < k \leq k_2$, then

$$A_k = k_1(\Delta R)^2 \sec \alpha \tan \beta \quad (55)$$

- If $k_2 < k$, then

$$A_k = \max(0, (\Delta R)^2 \sec \alpha [k_1 \tan \beta - (k - k_2 - 0.5) \tan \beta_1]) \quad (56)$$

in which the 'max' operator accounts for ranges where there are no hill clutter.

The clutter RCS is a function of range according to:

$$\sigma_c = \sigma_{total}^0 A_k \quad (57)$$

where σ_{total}^0 is given by (41). CNR is then computed by substituting $\sigma = \sigma_c$ of equation (57) into the radar equation (13).

For $\alpha = 30$ degrees, $\beta = 55$ degrees, $R_0 = 10$ NM, $\theta_a = 19.4$ degrees, $h_0 = 500$ m, distributed hill clutter profile is shown in Fig.36. The non-coherent summation of CNR and the noise floor of 0 dB is shown in Fig.36(a). For cases 1 and 2, the clutter level is 3 dB smaller than that of case 3. For ranges longer than 1 NM, the received power is at most -80 dBm for all three cases as shown in Fig.36(b). There is an abrupt drop in received clutter power at range 15 NM since there is no ground clutter return beyond the hill.

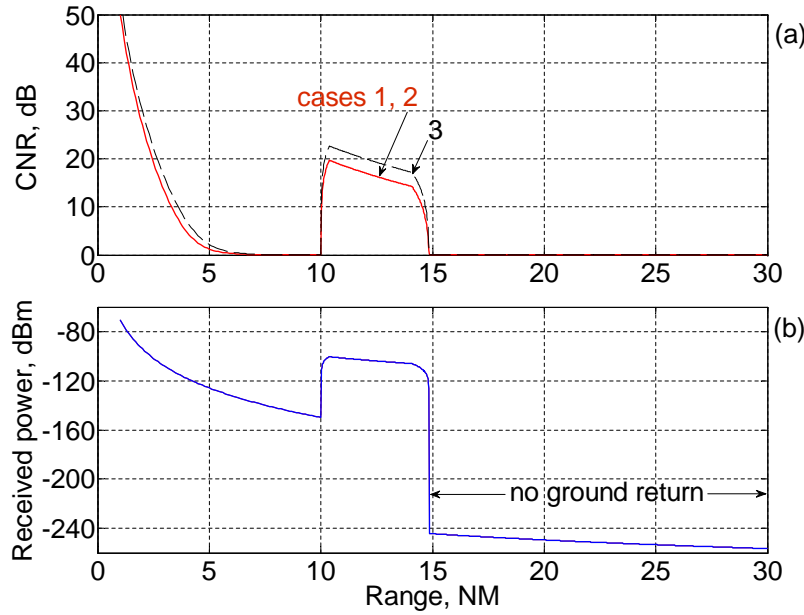


Figure 36: Distributed CNR and received power.

9.3 Comparison of Three PRF Cases.

- For case 1, as shown in Fig.36(a), CNR at the true range of 2 NM is 30 dB. Targets of interest which need to compete with this clutter are (i) those the true range of which is around 2 NM and, (ii) those the true range of which is between 10 to 20 NM and is in the first range ambiguity region.
 - (i) As shown in Fig.29, the worst clutter attenuation level is -34 dB at PRF=2 kHz. The worst clutter residue is $30 - 34 = -4$ dB. For targets of true range around 2 NM, the worst detection loss is approximately 1.5 dB which is the non-coherent summation of two random noise levels, one is 0 dB and one is -4 dB. As shown in Fig.26, a target with a small RCS of 1 m^2 has a high SNR of 32 dB at range around 2 NM. Therefore a detection loss of 1.5 dB will not cause any deleterious effect on target detection probability.
 - (ii) As shown in Fig.13 for PRF labels 1 to 4, at ranges in the first ambiguity interval closer than 20 NM there may exist targets which need to compete with clutter around 2 NM. The minimum of those four PRFs is 4737 Hz which corresponds to a clutter attenuation of approximately -38 dB as shown in Fig.29. The clutter residue is then $30 - 38 = -8$ dB. The worst detection loss is approximately 0.7 dB which is the non-coherent summation of two random noise levels, one is 0 dB and one is -8 dB.
- For case 2, there is no additional detection loss due to clutter residue since targets at a far range do not have to compete with clutter at a closer range.

- For case 3, the CNR around 2 NM is 33 dB (see Fig.36(a)) while the worst clutter attenuation level is -37 dB at PRF around 2 kHz (see Fig.29). The worst clutter residue is then -4 dB which is the same as that of case 1. As the PRFs of case 3 are approximately the same as those of case 1, the worst detection loss for case 3 is the same as that for case 1.

9.4 Summary.

The three cases are summarised in Table 14 in which the range resolution is 40 m. Case 1 is recommended for implementation since its frame-time is half of cases 2 and 3 while the detection loss is only 0.7 dB. If a finer velocity resolution is required for an improved tracking quality, then case 3 is recommended.

Table 14: Comparison of the three cases.

Case	Detection loss	Frame-time	Velocity resolution
1	0.7 dB	0.684 s	12.1 m/s
2	Nil	1.368 s	12.1 m/s
3	0.7 dB	1.368 s	6.0 m/s

10 Effect of a Sparse Array.

In practice, all the eight array columns may not be available for operation. A robust search algorithm should have the ability to cope with the effect of a sparse array where some channels are shut down. In this section, azimuth beam-forming for an 8-element linear array in which only five elements are working is addressed.

The full array configuration is shown in Fig.37(a). It is required that elements e_1 and e_8 at the two ends of the array must be kept. The beam-forming problem is to select the set of three elements $\{e_{k1}, e_{k2}, e_{k3}\}$ from the set $\{e_2, e_3, e_4, e_5, e_6, e_7\}$ such that for those beams formed with the set $\{e_1, e_{k1}, e_{k2}, e_{k3}, e_8\}$, both the 3 dB beam-width and the side-lobe level are minimised.

There are three optional configurations: (i) there is no gap between the set $\{e_{k1}, e_{k2}, e_{k3}\}$ and element e_1 as shown Fig.37(i) or, (ii) there is a gap as shown in Fig.37(ii), or (iii) there are one gap inside the set $\{e_{k1}, e_{k2}, e_{k3}\}$ and one gap between the set $\{e_{k1}, e_{k2}, e_{k3}\}$ and element e_1 as shown Fig.37(iii).

In order to have a low side-lobe level, window weights are applied such that the energy of the array should be concentrated in the elements at the centre of the array and faded in the elements near the two edges of the array [19]. For configuration (i), as the weights at elements e_5, e_6 , and e_7 are zero, the weight at e_8 should be small (i.e., in the neighbourhood of zero). As a result, there remain four elements available for beam-forming. For configuration (ii), as the weights at elements e_2, e_6 , and e_7 are zero, the weights at e_1 and e_8 should be in the neighbourhood of zero. As a result, there remain three elements

available for beam-forming. Similarly, for configuration (iii) there are three elements available for beam-forming. Therefore, configuration (i) is selected since beam-forming can be performed with four elements, compared with only three elements as in the other two configurations.

Beam-forming using configuration (i) and Chebyscheff weights is shown in Fig.38. These weights are only applied to the receiving beams. A side-lobe level of -25 dB is achieved, while the 3 dB beamwidth at boresight is approximately 30 degrees. The azimuth coverage is approximately 64 degrees, with three beam dwells per frame-time. For search operation the dwell sequence is scheduled as 1 – 2 – 3, where the numbers refer to the azimuth beam positions shown in Fig.38 and Table 15.

Target detection probabilities for array configuration (i) is shown in Fig.39. Target SNR is computed using radar equation (13) in which the antenna power is obtained from only four array columns instead of eight. It is observed that for PRF cases 1 and 2, only 80% detection probability can be achieved for targets of RCSs 1 and 100 m^2 at ranges 7 NM (around Parafield airport) and 20 NM (around Adelaide airport), respectively. For PRF case 3, a detection above 90% is still possible for the same scenario.

Therefore, PRF case 3 is preferable if the radar operates with only five array columns.

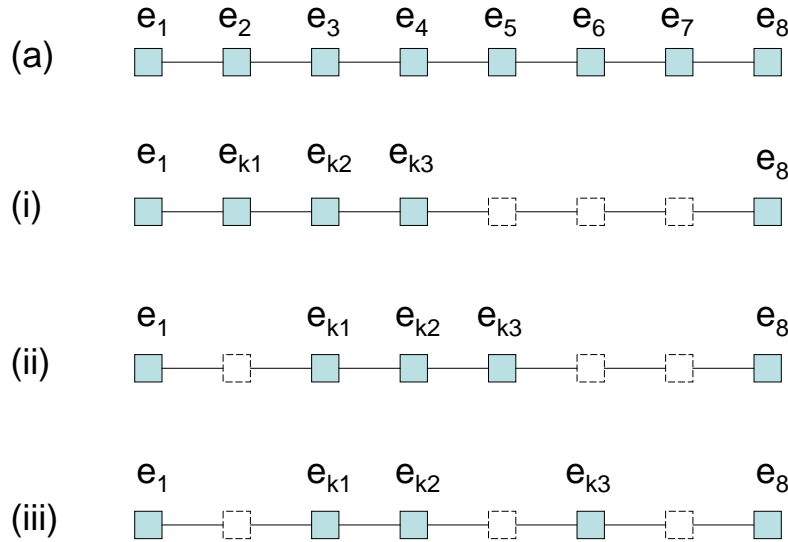


Figure 37: Array configurations.

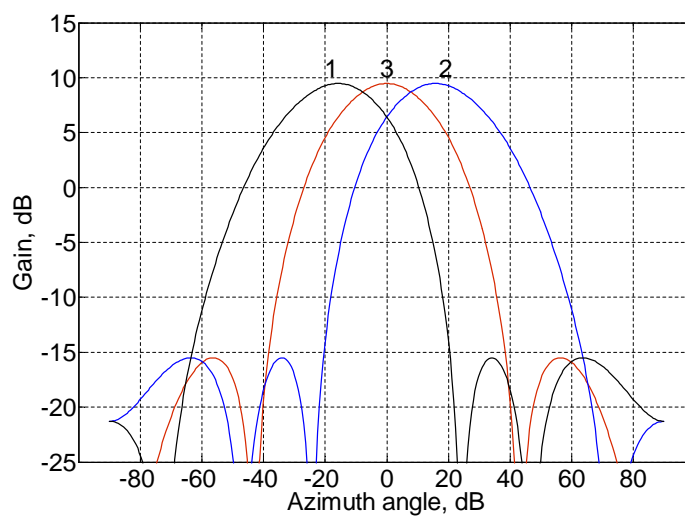


Figure 38: Sum channel beamforming with five antenna array columns (weights: 0.4827, 1.0000, 1.0000, 0.4827, 0.01).

Table 15: Beam direction θ and 3 dB beamwidth Θ_{3dB} for a 5-element linear array.

Direction label	1	2	3
θ , degrees	-15.7	15.7	0
Θ_{3dB} , degrees	32	32	30

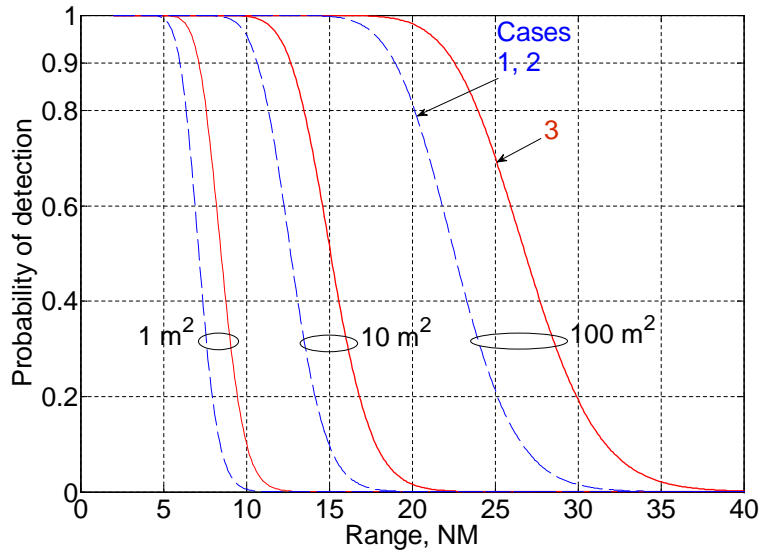


Figure 39: Target detection probability for array configuration (i), with 8 clear PRFs.

11 Alert-Confirm Search.

In this section, the possibility of a search mode design using a two-step sequential detector is discussed. Search operation, beam scheduling, and track-while-scan processing are described. Computations of false alarm rates and target detection probabilities are presented, and a comparison of the one-step detector with a two-step detector is given. Details of waveform and PRF selection using the major-minor PRFs technique are shown in Appendix E.

In a two-step sequential detector, two dwells are designed for each beam position. The first dwell is called the alert dwell, while the second dwell is called the confirm dwell. The confirm dwell is only made if there are detections (known as alerts) declared in the alert dwell. In other words, the confirm dwell only produces detection reports that correspond to the alert dwell. Due to the fluctuation of target signals, it is best to make the confirm dwell quickly using the same carrier frequency so that the signal detected in the alert step has not faded. Target detection probability is maximised if the time lag between the alert dwell and confirm dwell is shorter than the correlation time of the target [6].

For the alert dwell, all locations in a beam position are checked for target detection. For the confirm dwell, the sensitive locations are limited to a few locations in the vicinity of each alert.

The overall alert-confirm search operation is summarised as described below.

11.1 Search Operation.

- Alert: the antenna performs alert scan by stepping its beam over each of the nine beam positions in the following pattern:

$$1 - 2 - 3 - 4 - 5 - 6 - 7 - 8 - 9 - 1 - \dots \quad (58)$$

where the numbers denote the beam labels described in Fig.3. At each beam position in sequence (58), the radar transmits and receives a number of pulses of specified waveforms, PRFs, and carrier frequencies. The received data is then processed for target detection. If there are detections (also known as hits), i.e., there exist locations where the signal exceeds certain predefined thresholds, the search proceeds to the confirm step. Otherwise, the alert scan proceeds to the next beam position.

- Confirm: once hits are found, the hits are verified if they are new alerts, i.e., they are not the same hits produced by the previous alert beam and they do not come from targets already being tracked. If they are new alerts, then a second beam (also known as confirm beam) is transmitted and received at the azimuth position of the new alerts for confirmation. A new target is declared at each location of the new alerts where hypothesis H_1 is again verified. Otherwise (i.e., no new alerts), the search proceeds to the next alert beam position. If there are hits that belong to existing target tracks, measurements of those hits are used for track update.

The combined alert-confirm beams are scheduled as follows.

11.2 Beam Scheduling.

The antenna beams are scheduled for transmit-receive at the following discrete time slots determined by the radar controller:

$$t_0, t_1, \dots, t_k, t_{k+1}, \dots \quad (59)$$

One dwell is performed at each epoch $e_n = [t_n, t_{n+1}]$, $n = 0, 1, 2, \dots$. The quiescent frame-time is defined as the time it takes the antenna to scan its alert dwells over the search volume without the intervention of any confirm dwell.

The beam schedule consists of two lists, one for the schedule of alert dwells (and so the name a-list), and one for the schedule of confirm dwells (and so the name c-list). For transmit-receive, the c-list is of higher priority than the a-list.

The schedule of a dwell at time t_k is specified by the set $\{d_k(b_k), W_k, \beta_k\}$, i.e., a beam direction $b_k \in \{1, 2, \dots, 9\}$, the corresponding dwell time d_k , the set W_k of waveforms and PRFs in use, and the type of the dwell ($\beta_k = 0$ for alert dwell, 1 for confirm dwell). Those four parameters are determined by the search algorithm.

The combined alert-confirm beam scheduling is summarised as follows. Refer to the six steps described in Fig.40:

- (1) Assume that the current epoch is e_k , and the dwell to be executed is $\{d_k(b_k), W_k, \beta_k\}$. The time labels are:

- current time: $t = t_k$,
- the previous dwell finished at time $t^- = t_{k-1} + d_{k-1}$, which is also the start time for the processing of previously collected data,
- the current dwell will finish at time $t^+ = t_k + d_k$,
- (2) During the time interval $[t, t^+]$, two parallel operations are performed: current transmit-receive and continuing process of previously collected data (denoted as data received up to time t^-).
- (3) Once the transmit-receive has finished, the a-list and c-list are updated as follows:
 - After the execution of a dwell finishes:
 - * If an alert dwell has been executed, it is then re-scheduled to the lowest priority position in the a-list.
 - * If a confirm dwell has been executed, it is then removed from the c-list.
 - In addition, if the measurement of an alert hit from a previous time t_n ($n < k$) is reported, then there are three possibilities:
 - * (i) this measurement is verified to be associated with one of the targets already being tracked, then the measurement is passed to the tracker for updating the target track and no confirm dwell is scheduled for this alert;
 - * (ii) this measurement is verified to be associated with one of the previous alert hits already reported, then no confirm dwell is scheduled for this alert;
 - * (iii) this measurement is a new alert, i.e., neither (i) nor (ii) is verified, then the corresponding confirm dwell is added to the lowest priority position in the c-list.

By eliminating confirm dwells from existing targets as well as existing alerts, the frame-time can be kept to a minimal while maximising the detection probability of potentially new targets.

- (4) The dwell with the highest priority in the schedule is selected for the next epoch. The descending priority order is: from the top of the c-list to the end of the c-list, and then from the top of the a-list to the end of the a-list. Communication with the radar scheduler is then established for the next transmit-receive.
- (5) While waiting for the next dwell, the data collected up to time t^+ are processed.
- (6) Assume that time t_{k+1} is granted for the next dwell, the time labels are updated to:
 - current time: $t = t_{k+1}$,
 - previous data collected time finished at: $t^- = t_k + d_k$,
 - next data collected time will finish at: $t^+ = t_{k+1} + d_{k+1}$,

The process continues by repeating from step (2) of Fig.40.

An example of this process is given in Appendix F.

Since there is at most one confirm dwell to be scheduled for each alert dwell, the longest frame-time in the presence of new targets is approximately twice the quiescent frame-time (assume that on average, alert and confirm dwells have the same length).

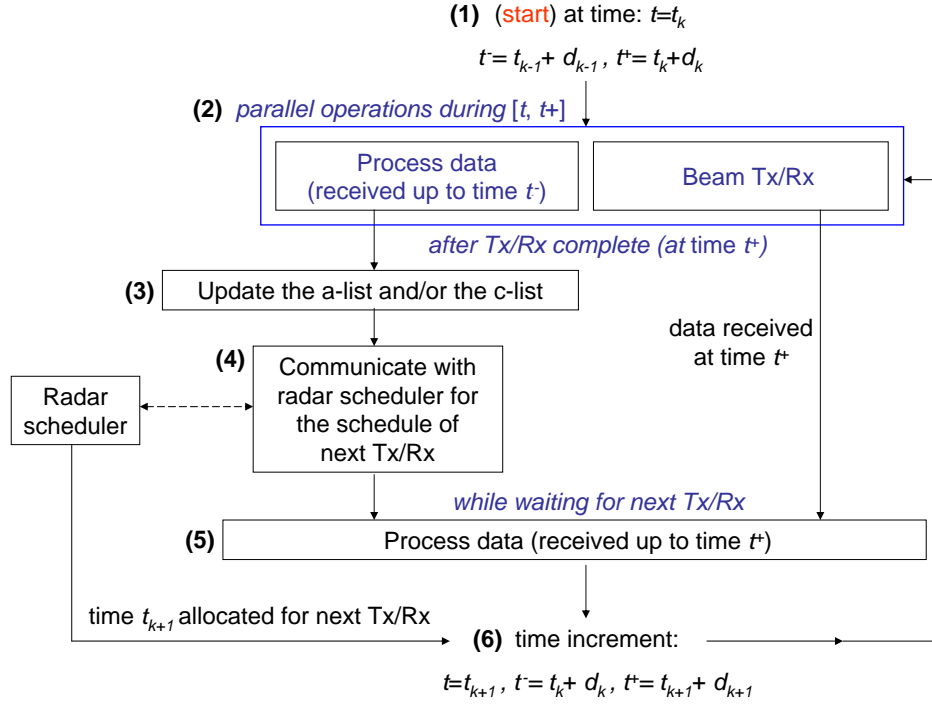


Figure 40: Overview of search mode operation with a two-step sequential detector.

11.3 Track-while-Scan Processing.

The data processing in step (2) of Fig.40 is described as follows.

11.3.1 Alert Processing.

Following the transmit-receive at each alert beam position, radar returns are processed by the Sum channel, the Difference channel, and the Guard channel. If no signal is detected (i.e., no hits), then alert scan continues; otherwise (i.e., with hits), the signals detected in the Sum channel are then compared with those at the same locations in the Guard channel in order to identify if the hits are from the main-lobe. If this is the case, then the hits are resolved for finer angle measurements using data from the Difference channel; otherwise (i.e., side-lobe hits), alert scan continues.

Measurements of hits, which include range, velocity, azimuth-elevation angles, and uncertainty, are then passed to the confirm decision logic. The main-lobe hits are verified if they are new hits by checking that they are neither hits from targets already being tracked nor hits previously reported from adjacent alert beams. In the case a main-lobe hit belongs to a target track, the new measurements are sent to the tracker for updating that track. The dashed lines in Fig.41 denotes the transfer of search results (i.e., target

measurements) to the tracker. If new alerts are verified, the search proceeds to the confirm step; otherwise, alert scan continues.

11.3.2 Confirm Processing.

At a revisit (i.e., confirm) beam position, the radar transmits a sequence of pulses of specified PRFs and waveforms for target confirmation. The same signal processing and signal detection procedure like that in the alert step is then performed up to the ‘measurements’ step of Fig.41, in which the Sum-Guard comparison step is by-passed. It is not necessary to perform Guard channel checking here since the hits to be confirmed are already verified (in the Alert step) to be in the main-lobe.

During a confirm revisit, only locations in the neighbourhoods of the alert hits are checked for target detection. If Sum channel hits are confirmed at locations in those neighbourhoods, measurements (obtained after finer angle resolving via the Difference channel) are then passed to the tracker. Alert scan then continues.

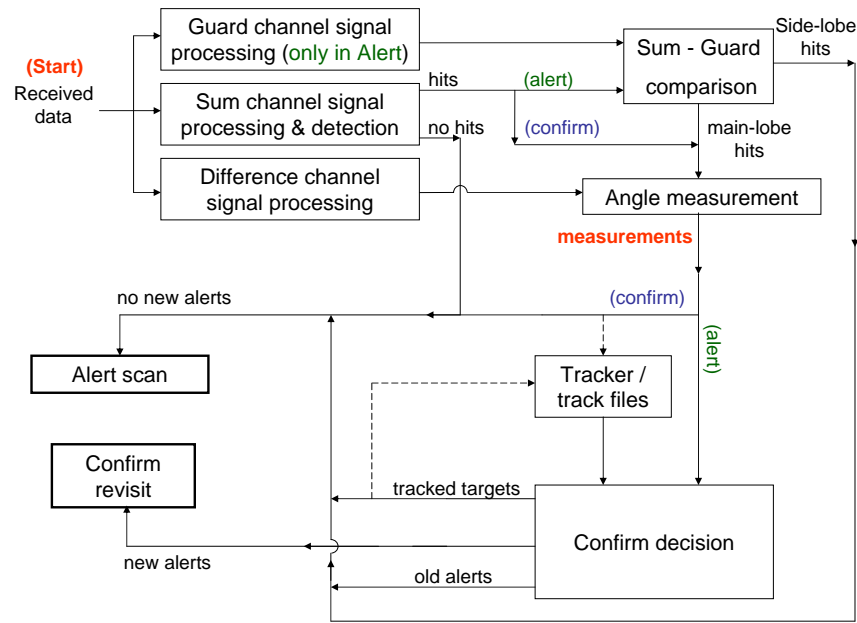


Figure 41: Overview of track-while-scan search with an alert-confirm detector.

11.4 False Alarm Rate & CA-CFAR Detection Threshold.

The CFAR threshold, either in the alert step or the confirm step, is set according to the following overall false alarm specifications:

- One confirm beam per t_c seconds.

- One false alarm reported per n_f seconds.

In the absence of target, the false detections in the alert step are independent from those of the confirm step. Therefore, at a beam position, the rate of output false alarm is [6], p70:

$$P_f = P_{f1} \times P_{f2} = [1 - (1 - P_{fa1})^{n_{d1}}] [1 - (1 - P_{fa2})^{n_{d2}}] \approx n_{d1} P_{fa1} n_{d2} P_{fa2} \quad (60)$$

where:

- P_{f1} is the ratio of the number of confirm beams to the number of alert beams performed during t_c seconds, i.e.,

$$P_{f1} = \frac{t_b}{t_c} \quad (61)$$

where t_b is the dwell time of an alert beam.

- P_{f2} is the ratio between: the number of confirm beams in which there is at least one detection, and the total number of confirm beams performed during n_f seconds, i.e.,

$$P_{f2} = \frac{t_c}{n_f} \quad (62)$$

- P_{fa1} and P_{fa2} are the false alarm rates per detection cell (i.e., the false alarm rates after the ‘Second threshold detection’ step described in Fig.7) in the alert step and the confirm step, respectively;
- n_{d1} and n_{d2} are the number of cell detections in one alert beam and one confirm beam, respectively. These two terms are computed as follows:

$$n_{d1} = \frac{(1 - D_u) c t_{f1}}{2\Delta R_1} \quad (63)$$

where D_u is the duty cycle, c is the speed of light, t_{f1} is the the length of one CPI in an alert beam, and ΔR_1 is the alert range resolution. Assume that the number of hits reported in an alert beam is n_{fa} , then:

$$\begin{aligned} n_{d2} &= n_{fa} \left(\frac{\Delta R_1}{\Delta R_2} + R_m \right) \left(\frac{\Delta V_1}{\Delta V_2} + 2D_m \right) \\ D_m &= \frac{t_d a_{max}}{\Delta V_2} \\ R_m &= \frac{t_d v_{max}}{\Delta R_2} \end{aligned} \quad (64)$$

where ΔR_2 is the confirm range resolution; $a_{max} = 2g \approx 20 \text{ m/s}^2$ is the maximum target acceleration; $v_{max} \approx 340 \text{ m/s}$ (Mach-1) is the maximum target velocity; ΔV_1 and ΔV_2 are the alert and confirm velocity resolutions, respectively; D_m and R_m account for the number of possible Doppler-walk and range-walk cells, respectively, due to the time delay t_d between an alert beam and the corresponding confirm beam.

The CA-CFAR false alarm rates F_{CA1} and F_{CA2} (of the alert step and confirm step, respectively) are computed by substituting $P_{fa} = P_{fa1}, P_{fa2}$ into equation (17) and solving the equation iteratively. The corresponding CA-CFAR detection threshold multipliers T_1 and T_2 (of the alert step and confirm step, respectively) are then computed using equation (14) in which $F_{CA} = F_{CA1}, F_{CA2}$.

11.5 Computation of Target Detection Probability.

At a beam position, the detection probability of the alert-confirm detection procedure is [6] pp66-71:

$$P = P_1 P_2|_{Alert} \quad (65)$$

where P_1 is the detection probability of the alert step; and $P_2|_{Alert}$ is the detection probability of the confirm step, conditioned on the reported alert.

In general, the number of cell detections in the confirm step is much smaller than that in the alert step, i.e., $n_{d2} \ll n_{d1}$ (eg., $60 \ll 28500$ as shown in Table E2 and Table E3 of Appendix E). Therefore, a much lower CFAR detection threshold can be set for the confirm step. With enough target SNR and while the alert-confirm time delay is shorter than the target correlation time, using the same waveform and carrier frequency in both steps, the overall alert-confirm target detection probability often approaches the alert detection probability [6], i.e.,

$$P = P_1 P_2|_{Alert} \approx P_1 \quad (66)$$

In case the alert-confirm time delay is longer than the target correlation time, the detection probabilities of the two steps are uncorrelated. The overall alert-confirm target detection probability is then:

$$P = P_1 P_2 \quad (67)$$

where P_1 and P_2 are the target detection probability of the alert step and the confirm step, respectively.

The target correlation time is given by [6], p66:

$$t_{corr} = \frac{\lambda}{2\omega_a L_x} \quad (68)$$

where λ is the wavelength, ω_a is the target rotation rate about the line of sight, and L_x is the dimension of the target normal to the line of sight and the axis of rotation. For a typical aircraft case, ω_a is a few hundredths of radians per second while L_x can be 10 to a few tens of metres. Then with an L-band wavelength of 0.23 metres, t_{corr} can be between 0.1 seconds to 0.4 seconds.

Typical alert-confirm target detection probability curves are shown in Fig.42 for three target RCS values. The curves are plotted for the case when the major-minor PRF scheduling technique (which will be discussed later) is employed. It is observed that the detection range at 90% detection probability can be extended up to three nautical miles further if confirm revisits are made within the target correlation time.

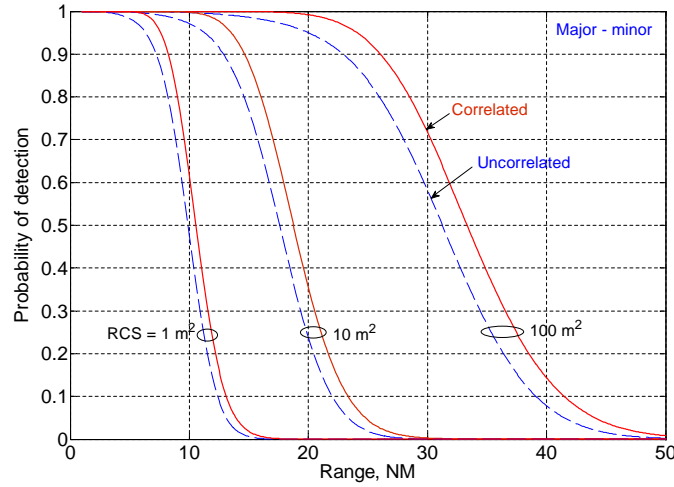


Figure 42: Alert-confirm target probability of detection.

11.6 Waveforms and PRFs Design.

In a two-step sequential detector, there are two main techniques of PRF selection for resolving range and velocity ambiguities: the M -of- N method and the major-minor method.

For the M -of- N method, namely the 3-of-8 combination, eight PRFs are employed in the alert step. If at least three hits are found in three of those eight PRFs, a target is suspected. Those three PRFs are then used to resolve the range and velocity ambiguities of the suspected target. In the confirm step, any one of these three PRFs can be used for target confirmation.

For the major-minor method, target range and velocity ambiguities are resolved over the two detection steps of the alert-confirm detector. In the first step, three major PRFs are employed. Once a hit is found in one of the major PRFs, the search proceeds to the second step in which another two minor PRFs are then used for range-velocity ambiguity resolving. A total of nine PRFs are required: three major PRFs and three pairs of minor PRFs, in which each pair is designed for use with a particular major PRF [18].

As the 3-of-8 technique has been presented in the above one-step detector, the major-minor technique is now considered for the two-step detector. See Appendix E for details of the designed waveforms and PRFs.

11.7 Comparison of One-step and Two-step Detectors.

In this section, the detection performance and beam scheduling complexity of the one-step search are compared with those of the two-step search.

11.7.1 Detection Performance.

In Fig.43, detection curves for the one-step and two-step detectors are shown at one false detection per minute. The false confirm rate of the two-step detector is set to one per 30 seconds.

- The one-step is realised with a dwell time of 0.076 s, which consists of 8 CPIs, each of which is $0.076/8 = 0.0095$ s. The 3-of-8 binary detector is applied.
- The two-step is realised with an alert dwell time of 0.076 s, which consists of 3 CPIs, each of which is $0.076/3 \approx 0.025$ s (the 1-of-3 binary detector is applied). The confirm dwell time is 2×0.076 s, which consists of 2 CPIs, each of which is 0.076 s (2-of-2 binary detector is applied).
- For the one-step detector, the range resolution is either 40 m or 200 m, while the velocity resolution is 12 m/s. For the two-step detector, the range resolution is 40 m, while the velocity resolution is 1.5 m/s. The velocity resolution of the one-step is 8 times coarser than that of the two-step.

As shown in Fig.43, when the confirm dwell is made within the target correlation time, the two-step detector gives the highest detection probability. However, when the confirm dwell is made after the target correlation time has elapsed, the one-step detector gives superior detection performance if a detection probability above 90% is required.

With the same false alarm setting as above, Fig.44 shows the detection curves of the one-step and two-step detectors which give the same range resolution of 40 m and the same velocity resolution of 1.5 m/s. The one-step detector is realised using a dwell time of 3×0.076 s, which consists of three CPIs each of which is 0.076 s (the 3-of-3 binary detector is applied). The two-step is realised as described above. It is observed that the two-step out-performs the one-step, even if the confirm dwell is made after the correlation time has elapsed. Although not shown here, it is found that the two-step is up to 3 dB better than the one-step if detection probabilities above 90% are required.

11.7.2 Beam Scheduling Complexity.

For the one-step detector, the beam scheduling algorithm is simple and straight-forward for implementation since no interaction with the tracker is required. For the two-step detector, the beam scheduling requires feedback from the tracker as shown in Fig.41. Without this feedback loop, a confirm dwell may need to be made for each of the targets which are already being tracked. This may cause the frame time to be longer than necessary. The design of a feedback loop to ensure that a confirm beam is made only for the confirmation of new targets is a worthwhile investigation for future research.

12 Conclusions.

A track-while-scan search using a one-step detection algorithm is proposed for initial implementation in the XPAR-2 radar system. Details of target detection performance analysis are presented.

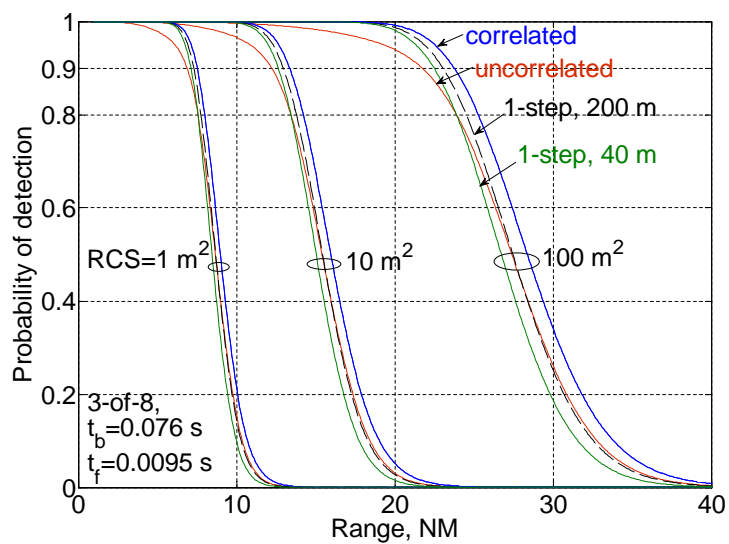


Figure 43: One-step detection vs two-step detection at one false alarm per minute.

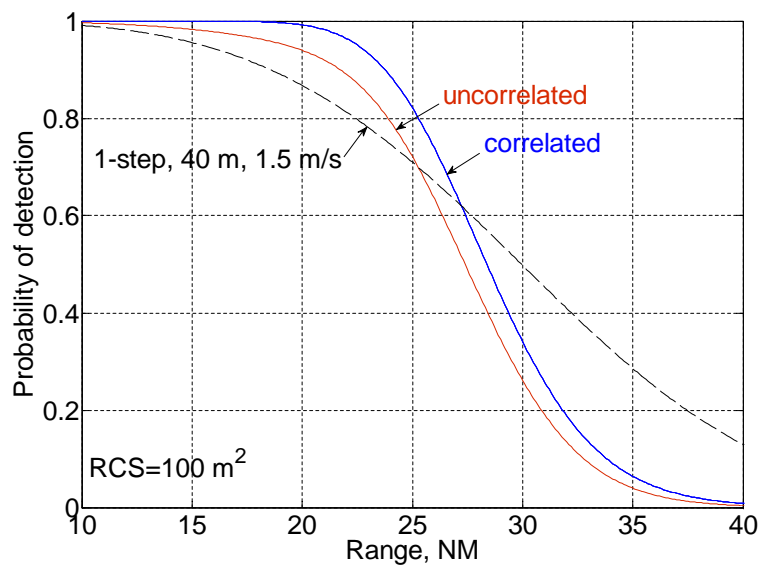


Figure 44: One-step detection vs two-step detection with the same velocity resolution.

Three options for waveform and PRF selections are analysed. In option 1, there is one set of 8 PRFs which are designed for detection of targets between 2 NM to 20 NM. In option 2, there are two separate PRF sets (each consists of 8 PRFs), which are designed such that one is optimised for close range targets between 2 NM to 7 NM, and one is optimised for targets between 7 NM to 20 NM. Option 3 is similar to option 1, the only difference is that the CPI of option 3 is twice that of option 1. Due to the limitation of target detection caused by phase noise and clutter, option 3 is proposed for implementation.

In the presence of strong clutter discretises, it is anticipated that on the radar screen there may exist isolated regions of high contrast at which targets may not be detected.

A combined track-while-scan search and two-step detection is also analysed. The analysis shows that an improvement of approximately 3 dB in detection sensitivity can be achieved compared with the conventional one-step detection. However, the beam scheduling for a two-step detector is more complex than that of the one-step detector. This beam scheduling design is a worthwhile topic for future research.

Acknowledgements.

The author would like to thank Mr. Robert K. Young for his valuable input to this search mode design project and report. Thanks are directed to Mr. Richard Langdon for his guidance through many of the practical aspects of radar search mode design as well as his valuable input to this report.

Appendix A Computation of the Longest CPI.

For a CPI of length t_f , the width of the velocity resolution cell is:

$$\Delta V = \frac{\lambda}{2t_f} \quad (\text{A1})$$

where λ is the radar wavelength. The time it takes a target with a maximum acceleration of $2g$ to go out of this velocity resolution cell is:

$$t_{out} = \frac{\Delta V}{2g} = \frac{\lambda}{4gt_f} \quad (\text{A2})$$

The longest CPI should be shorter than the time t_{out} , i.e.,

$$t_f \leq t_{out} = \frac{\lambda}{4gt_f} \quad (\text{A3})$$

which is equivalent to:

$$t_f \leq \sqrt{\frac{\lambda}{4g}} \quad (\text{A4})$$

For $\lambda = 0.23$ m, $g = 9.8$ m/s²: $t_f \leq 0.076$ s.

Appendix B Experimental Phase Noise.

Phase noise in the XPAR-2 system was experimentally characterised, and a descriptive plot was shown in Fig.B1 [21].

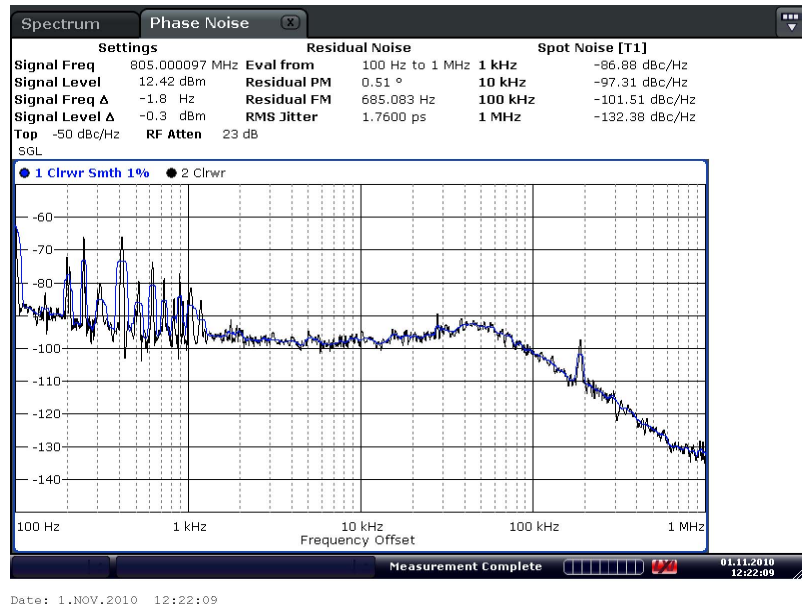


Figure B1: An experimental oscillator phase noise spectrum [21].

Appendix C Parameters of Land Surface.

Parameters of land surface for constant- γ model are given in Table C1 for different surface types [6], p111. The mean reflectivity coefficient γ is in dB; the rms height deviation σ_h is in metres; and the slope β_0 is in radians.

Table C1: *Parameters of land surface for constant- γ model.*

Surface type	γ , dB	σ_h , m	β_0 , radian
Mountain	-5	100	0.1
Urban	-5	10	0.1
Wooded hill	-10	10	0.05
Rolling hills	-12	10	0.05
Desert	-15	3	0.03
Flatland	-20	1	0.02
Smooth surface	-25	0.3	0.01

Appendix D Computation of Hill Clutter Area and Grazing Angle.

Refer to Fig.35 which is redrawn here as Fig.D1 for convenience. Let $R = R_0$ which is the distance from the radar to point A, which is the intersection between the hill-ground border and the near edge of the radar 3 dB beamwidth. Denote the first hill-clutter patch at range $R + \Delta R$ as A_1 which is the area S_1 of the triangular AHB. The second hill-clutter patch at range $R + 2\Delta R$, denoted as A_2 , is area of the trapezium HBCK which is equal to the area S_2 of the triangular AKC subtracted by the area of the first hill-clutter patch S_1 . In general, the hill-clutter area A_k at range $R + k\Delta R$, $k = 2, 3, \dots$, is:

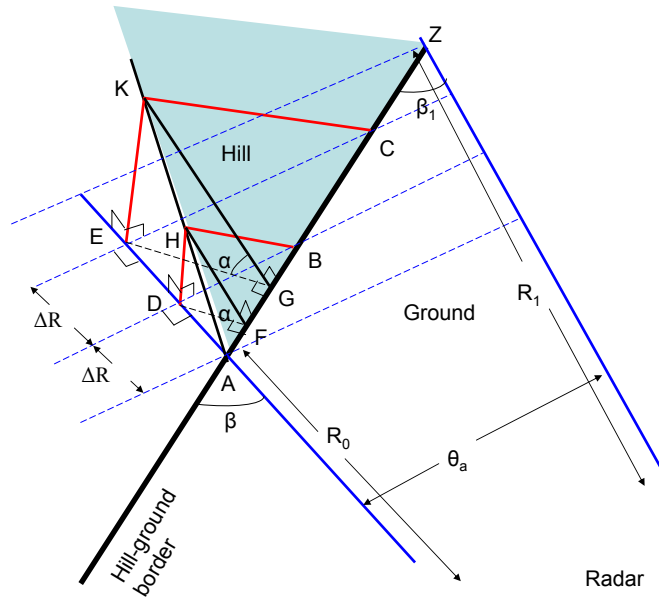


Figure D1: Hill clutter geometry in 3-D view.

$$A_k = S_k - S_{k-1} \quad (D1)$$

where S_k is the area of the triangular formed on the hill at range $R + k\Delta R$.

The area of the triangular AHB is:

$$\begin{aligned} S_1 &= HF \times AB / 2 \\ &= (DF \times \sec \alpha) \times (\Delta R \times \sec \beta) / 2 \\ &= (\Delta R \times \sin \beta \times \sec \alpha) \times (\Delta R \times \sec \beta) / 2 \\ &= 0.5(\Delta R)^2 \sec \alpha \tan \beta \end{aligned} \quad (D2)$$

Similarly, the area S_k , $k = 2, 3, \dots$, is:

$$S_k = 0.5(k\Delta R)^2 \sec \alpha \tan \beta \quad (\text{D3})$$

The hill-clutter area A_1 (at range $R + \Delta R$) is:

$$A_1 = S_1 = 0.5(\Delta R)^2 \sec \alpha \tan \beta \quad (\text{D4})$$

The hill-clutter area A_k (at range $R + k\Delta R$, $k = 2, 3, \dots$) is:

$$\begin{aligned} A_k &= S_k - S_{k-1} \\ &= [(k\Delta R)^2 \sec \alpha \tan \beta / 2] - [(k-1)\Delta R)^2 \sec \alpha \tan \beta / 2] \\ &= (k - 0.5)(\Delta R)^2 \sec \alpha \tan \beta \end{aligned} \quad (\text{D5})$$

- If $k \leq k_1$, then

$$A_k = (k - 0.5)(\Delta R)^2 \sec \alpha \tan \beta \quad (\text{D6})$$

- If $k_1 < k \leq k_2$, then

$$\begin{aligned} A_k &= (k - 0.5)(\Delta R)^2 \sec \alpha \tan \beta - (k - k_1 - 0.5)(\Delta R)^2 \sec \alpha \tan \beta \\ &= k_1(\Delta R)^2 \sec \alpha \tan \beta \end{aligned} \quad (\text{D7})$$

- If $k_2 < k$, then

$$\begin{aligned} A_k &= k_1(\Delta R)^2 \sec \alpha \tan \beta - (k - k_2 - 0.5)(\Delta R)^2 \sec \alpha \tan \beta_1 \\ &= (\Delta R)^2 \sec \alpha (k_1 \tan \beta - (k - k_2 - 0.5) \tan \beta_1) \end{aligned} \quad (\text{D8})$$

The grazing angle from the radar to the hill surface is computed as follows. Refer to Fig.D2 in which the radar is at point O . The 3 dB azimuth beam intersects with the hill-ground border at point A at which the range is $OA = R$. OH is perpendicular to the hill surface, while OB is perpendicular to the hill-ground border.

Let θ be the angle between AO and AH , the following relations hold:

$$\begin{aligned} \sin \theta &= \frac{OH}{R} \\ &= \frac{OB \sin \alpha}{R} \\ &= \frac{(R \sin \beta) \sin \alpha}{R} \\ &= \sin \alpha \sin \beta \end{aligned} \quad (\text{D9})$$

Appendix E Alert-Confirm Waveform and PRF Parameters.

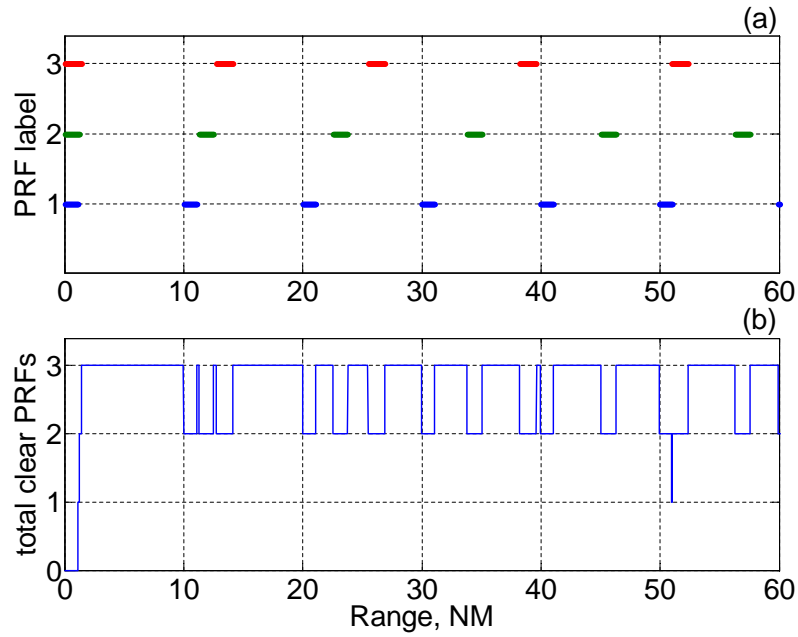
The alert-confirm major waveform characteristics are summarised in Table E1, while details of major PRF selections are shown in Table E2. The alert range blind zone plots are shown in Fig.E1. There are 3 clear PRFs (which is the maximum) between 2 NM and 10 NM (around Parafield airport) and between 13 NM to 20 NM (around Adelaide airport). The first velocity ambiguity is at 660 m/s (greater than Mach-1) as evident in the velocity blind zone plots of Fig.E2. The alert-confirm minor waveform characteristics are summarised in Table E3. In the confirm range blind zone plots shown in Fig.E3, each of the first range blind zones of the minor pairs are shifted to between 4 to 7 range resolution cells (each resolution cell is 40 m). A shift of at least 2 range resolution cells is required for resolving range ambiguity [18].

Table E1: Alert-confirm waveform characteristics.

Duty cycle	0.10
Number of alert PRFs	3
Carrier gap, MHz	15
Alert dwell, s	0.076
Alert CPI, s	0.0253
Alert range resolution, m	120
Alert velocity resolution, m/s	4.6
Alert LFM bandwidth, MHz	1.25
Alert velocity blind-zone width, m/s	12.2
Confirm dwell, s	2×0.076
Confirm CPI, s	0.076
Confirm range resolution, m	40
Confirm velocity resolution, m/s	1.5
Confirm LFM bandwidth, MHz	3.75
Confirm velocity blind-zone width, m/s	6

Table E2: Alert-confirm major PRFs.

PRF, Hz	7302	6474	5724
Carrier frequency, MHz	1285	1300	1315
Pulse-width, μs	13.695	15.446	17.470
R_u , NM	9.98	11.26	12.73
Δ_r , NM	1.11	1.25	1.41
V_u , m/s	842.5	747.0	660.5
Doppler cells	185	164	145
Range cells	154	174	197
RD cells	28490	28536	28565
Number of cell detections n_{d1}	28490	28536	28565
Compression ratio	17	19	22

**Figure E1:** Range blind-zone plot of major PRFs.

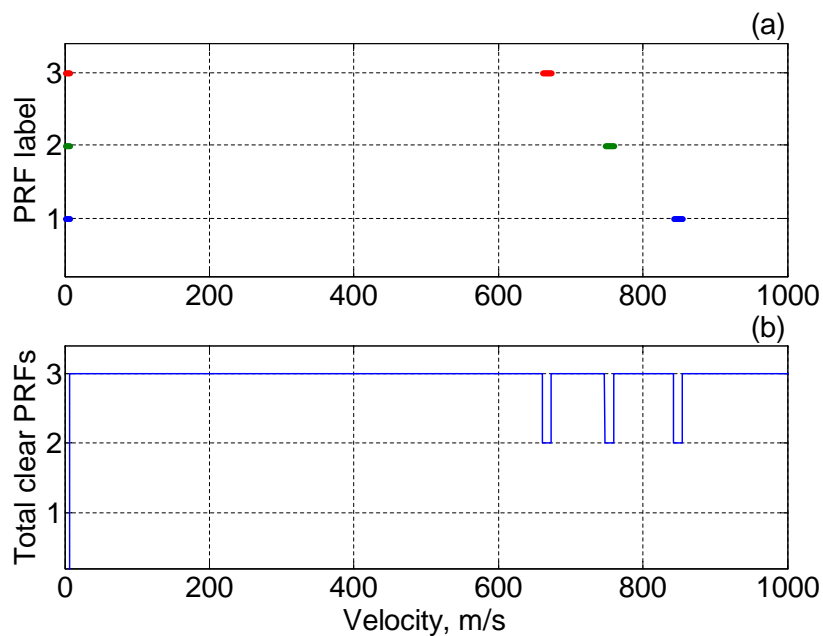


Figure E2: Velocity blind-zone plot of major PRFs.

Table E3: Alert-confirm minor PRFs.

Alert major PRFs, Hz	7302		6474		5724	
Confirm minor PRFs, Hz	7368	7447	6526	6593	5776	5855
Carrier frequency, MHz	1285	1285	1300	1300	1315	1315
Uncompressed pulse-width, μs	13.572	13.428	15.323	15.168	17.313	17.079
Blind range, NM	9.89	9.79	11.17	11.02	12.57	12.40
Range blind zone width, NM	1.10	1.09	1.24	1.23	1.40	1.38
Blind velocity, m/s	850.2	859.3	753.0	760.6	666.6	675.7
Doppler cells	187	189	165	167	146	148
Range cells	153	151	172	170	194	191
RD cells	28611	28539	28380	28390	28324	28268
Number of cell detections n_{d2}	60	60	60	60	60	60
Compression ratio	51	51	57	57	65	65

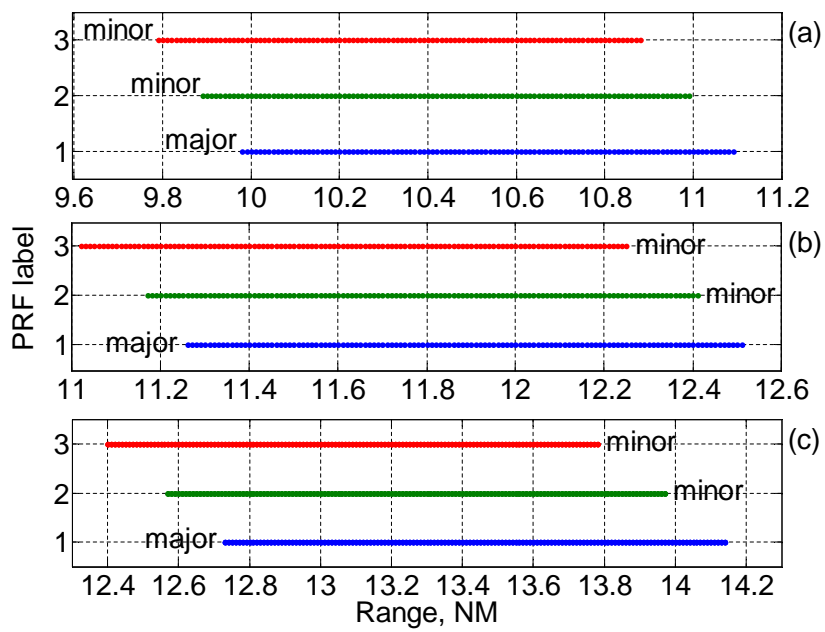


Figure E3: Range blind-zone plot of major-minor PRFs.

Appendix F An Illustration Example of Alert-Confirm Beam Scheduling.

- At epoch e_1 , i.e., the beginning of the search operation:
 - Step (1). The time labels are: $t = t_1 = 0$, $t^- =$ not applied, and $t^+ = d_1$. The a-list consists of the schedule for a full alert frame-time, i.e., the queue of the dwells in the a-list is:

$$a_1 - a_2 - a_3 - a_4 - a_5 - a_6 - a_7 - a_8 - a_9 \quad (\text{F1})$$

where the letter a denotes an alert dwell; and the numbers refer to the beam positions shown in Fig.3. The c-list is empty.

- Step (2). Dwell a_1 at the top of the a-list is executed.
- Step (3). After dwell a_1 has been executed, it is re-scheduled to the end of the a-list, i.e., the queue in the a-list is:

$$a_2 - a_3 - a_4 - a_5 - a_6 - a_7 - a_8 - a_9 - a_1 \quad (\text{F2})$$

- Step (4). Communication with the radar scheduler is established for the schedule of dwell a_2 (which is on the top of the a-list) in the next epoch.
- Step (5). Data collected at time t^+ is processed.
- Step (6). Time t_2 is allocated for epoch e_2 , and the time labels are updated as: $t = t_2$, $t^- = d_1$, and $t^+ = t_2 + d_2$.

- At epoch e_2 :
 - Step (2). The c-list is empty. The dwell a_2 at the top of the a-list (F2) is executed.
 - Step (3). After dwell a_2 has been executed, it is re-scheduled to the end of the a-list, i.e., the queue in the a-list is:

$$a_3 - a_4 - a_5 - a_6 - a_7 - a_8 - a_9 - a_1 - a_2 \quad (\text{F3})$$

Assume that results from data processing is not yet available, then the c-list is still empty.

- Step (4). Communication with the radar scheduler is established for the schedule of dwell a_3 in the next epoch.
- Step (5). Data collected up to time t^+ is processed.
- Step (6). Time t_3 is allocated for epoch e_3 , and the time labels are updated as: $t = t_3$, $t^- = t_2 + d_2$, and $t^+ = t_3 + d_3$.

- At epoch e_3 :
 - Step (2). The c-list is empty. Dwell a_3 at the top of the a-list (F3) is executed.

- Step (3). After dwell a_3 has been executed, it is re-scheduled to the end of the a-list, i.e., the queue in the a-list is:

$$a_4 - a_5 - a_6 - a_7 - a_8 - a_9 - a_1 - a_2 - a_3 \quad (\text{F4})$$

Assume that results from data processing show two new alerts, firstly at beam position 1 and secondly at beam position 2, then two confirm dwells are added to the c-list: c_1 first, and c_2 second to c_1 . The queue in the c-list is:

$$c_1 - c_2 \quad (\text{F5})$$

- Step (4). Communication with the radar scheduler is established for the schedule of dwell c_1 which is at the top of the c-list in the next epoch.
- Step (5). Data collected up to time t^+ is processed.
- Step (6). Time t_4 is allocated for epoch e_4 , and the time labels are updated as: $t = t_4$, $t^- = t_3 + d_3$, and $t^+ = t_4 + d_4$.

- At epoch e_4 :

- Step (2). Dwell c_1 is executed.
- Step (3). After dwell c_1 has been executed, it is removed from the c-list (F5), i.e., the queue in the c-list is:

$$c_2 \quad (\text{F6})$$

Since no alert dwell is executed in this epoch, the queue in the a-list is the same as in (F4). Assume that results from data processing show no new alerts, the queue in the c-list is the same as in (F6).

- Step (4). Communication with the radar scheduler is established for the schedule of dwell c_2 (which is at the top of the c-list) in the next epoch.
- Step (5). Data collected up to time t^+ is processed.
- Step (6). Time t_5 is allocated for epoch e_5 , and the time labels are updated as: $t = t_5$, $t^- = t_4 + d_4$, and $t^+ = t_5 + d_5$.

- At epoch e_5 :

- Step (2). Dwell c_2 is executed.
- Step (3). After dwell c_2 has been executed, it is removed from the c-list (F6), i.e., the c-list is now empty. Since no alert dwell is executed in this epoch, the queue in the a-list is the same as in (F4). Assume that results from data processing show no new alerts, the c-list remains empty.
- Step (4). Communication with the radar scheduler is established for the schedule of dwell a_4 , which is at the top of the a-list (F4), in the next epoch.
- Step (5). Data collected up to time t^+ is processed.
- Step (6). Time t_6 is allocated for epoch e_6 , and the time labels are updated as: $t = t_6$, $t^- = t_5 + d_5$, and $t^+ = t_6 + d_6$.

- At epoch e_6 :

- Step (2). Dwell a_4 is executed.
- Step (3). After dwell a_4 has been executed, it is re-scheduled to the end of the a-list, i.e., the queue in the a-list is:

$$a_5 - a_6 - a_7 - a_8 - a_9 - a_1 - a_2 - a_3 - a_4 \quad (\text{F7})$$

Assume that results from data processing show no new alerts, the c-list remains empty.

- Step (4). Communication with the radar scheduler is established for the schedule of dwell a_5 , which is at the top of the a-list (F7), in the next epoch.
 - Step (5). Data collected up to time t^+ is processed.
 - Step (6). Time t_7 is allocated for epoch e_7 , and the time labels are updated as: $t = t_7$, $t^- = t_6 + d_6$, and $t^+ = t_7 + d_7$.
- And so on . . .

References

1. Richards, M.A., Scheer, J.A., and Holm, W.A., 'Principles of Modern Radar, Volume 1: Basic Principles', Sci-Tech Publishing Company, 2010.
2. Blackman, S. and Popoli, R., 'Design and Analysis of Modern Tracking Systems', Artech House, 1999, USA.
3. Bar-Shalom, T. and Li, X-R, 'Multitarget-Multisensor Tracking: Principles and Techniques', Storrs, CT: YBS Publishing, 1995.
4. DiFranco, J.V., 'Radar Detection', Artech House, 1980, USA.
5. Barton, D.K., 'Modern Radar System Analysis', Artech House, 1998, USA.
6. Barton, D.K., 'Radar System Analysis and Modeling', Artech House, 2005, USA.
7. Zhen, D., A survey of radar resource management algorithms, Proc. of the Canadian Conference on Electrical and Computer Engineering, pp1559-1564, 2008.
8. White, K., Williams, J., and Hoffensetz, P., Radar sensor management for detection and tracking, Proc. of the 11th International Conference on Information Fusion, pp. 1-8, 2008.
9. Suvorova, S., Howard, S.D., and Moran, W., Beam and waveform scheduling approach to combined radar surveillance and tracking - the Paranoid Tracker, in Proc. 2nd Int. Conf. Waveform Diversity and Design, Hawaii, Jan 2006.
10. Crowder, D.A., 'Google Earth for Dummies', Wiley Publishing, 2006, USA.
11. Langdon, R., 'XPAR-2 System Concept' (XPAR-2 Documents, Microwave Radar Branch, EWRD, DTSO, 2010.)
12. Langdon, R., 'H1 Antenna' (XPAR-2 Documents, Microwave Radar Branch, EWRD, DTSO, 2012.)
13. Balanis, C.A., 'Antenna Theory', 3rd edn, John Wiley & Sons, 2005, USA.
14. Maisel, L., Performance of side-lobe blanking systems, IEEE Transactions on Aerospace & Electronic Systems, 1968, Vol. 4, No.2 , pp174-180.
15. Burger, W. and Nickel, U., Space-time adaptive detection for airborne multifunction radar, in Proceedings of the 2008 IEEE Radar Conference, IEEE Conference Publications, pp1-5.
16. Schnidman, D.A. and Toumodge, S.S., Side-lobe blanking with integration and target fluctuation, IEEE Transactions on Aerospace & Electronic Systems, 2002, Vol. 38, No.3, pp1023-1037.
17. Langdon, R., 'H2.3 Array Controller Notes' (XPAR-2 Documents, Microwave Radar Branch, EWRD, DTSO, 2010.)

18. Morris, G., 'Airborne pulsed Doppler radar systems', 2nd edn, Artech House, 1996, USA.
19. Mahafza, B.R., 'Radar Systems Analysis and Design Using Matlab', Chapman & Hall/CRC, 2005, USA.
20. Gandhi, P.P. and Kassam, S.A., Analysis of CFAR processors in nonhomogeneous background, IEEE Transactions on Aerospace & Electronic Systems, 1988, 24, (4), pp427-445.
21. Langdon, R., 'H2-2 Transceiver Notes' (XPAR-2 Documents, Microwave Radar Branch, EWRD, DTSO, 2012.)
22. Ward, H.R., A model environment for search radar evaluation, IEEE EASCON 71 Record, 1971, IEEE Inc., pp164-171.

DEFENCE SCIENCE AND TECHNOLOGY ORGANISATION DOCUMENT CONTROL DATA				1. CAVEAT/PRIVACY MARKING	
2. TITLE XPAR-2 Search Mode Initial Design			3. SECURITY CLASSIFICATION Document (U) Title (U) Abstract (U)		
4. AUTHOR T.V. Cao			5. CORPORATE AUTHOR Defence Science and Technology Organisation PO Box 1500 Edinburgh, South Australia 5111, Australia		
6a. DSTO NUMBER DSTO-TR-2904		6b. AR NUMBER AR-015-766		6c. TYPE OF REPORT Technical Report	
7. DOCUMENT DATE November, 2013					
8. FILE NUMBER 2013/1200084/1		9. TASK NUMBER DST 07/213		10. TASK SPONSOR CDS	
11. No. OF PAGES 78		12. No. OF REFS 22			
13. URL OF ELECTRONIC VERSION http://www.dsto.defence.gov.au/publications/scientific.php			14. RELEASE AUTHORITY Chief, National Security and ISR Division		
15. SECONDARY RELEASE STATEMENT OF THIS DOCUMENT <i>Approved for Public Release</i> OVERSEAS ENQUIRIES OUTSIDE STATED LIMITATIONS SHOULD BE REFERRED THROUGH DOCUMENT EXCHANGE, PO BOX 1500, EDINBURGH, SOUTH AUSTRALIA 5111					
16. DELIBERATE ANNOUNCEMENT No Limitations					
17. CITATION IN OTHER DOCUMENTS No Limitations					
18. DSTO RESEARCH LIBRARY THESAURUS Search mode Alert-confirm search Constant false alarm rate Radar detection					
19. ABSTRACT In this report, the initial design of a search mode for the Experimental Phased-Array Radar 2 (XPAR-2) system developed at DSTO is addressed. A track-while-scan search method combined with a one-step detection algorithm is proposed for implementation. Effects of discrete and distributed land clutter on detection performance are analysed. Limitation of clutter attenuation due to oscillator phase noise is addressed. Three options for waveform and pulse repetition frequency (PRF) selections are considered. Option 1 consists of 8 PRFs which are designed for detection of targets between 2 NM to 20 NM. Option 2 consists of two separate PRF sets (each consists of 8 PRFs), which are designed such that one is optimised for close range targets between 2 NM to 7 NM, and one is optimised for targets between 7 NM to 20 NM. Option 3 is similar to option 1, but with twice the coherence processing interval. In all three options, the 3-of-8 binary detection rule is applied. Option 3 is selected for initial implementation. A track-while-scan search regime combined with a sequential alert-confirm detection algorithm is considered for future research study.					